FY 2014 Status Report: Using Finite Model Analysis and Out of Hot Cell Surrogate Rod Testing to Analyze High Burnup Used Nuclear Fuel Mechanical Properties

Fuel Cycle Research & Development

Prepared for
U.S. Department of Energy
Used Fuel Disposition Campaign
J.-A. Wang, H. Jiang, H. Wang
B. B. Bevard, and J. M. Scaglione
Oak Ridge National Laboratory

OAK RIDGE NATIONAL LABORATORY
MANAGED BY UT-BATTELLE FOR THE U.S. DEPARTMENT OF ENERGY

Materials Science and Technology Division
Oak Ridge National Laboratory

FY 2014 Status Report: Using Finite Model Analysis and Out of Hot Cell Surrogate Rod Testing to Analyze High Burnup Used Nuclear Fuel Mechanical Properties

Jy-An John Wang, Hao Jiang, and Hong Wang

Program Managers
Bruce Bevard and John Scaglione

Date Published: August 2014

SUMMARY

Finite element analysis (FEA) was utilized to analyze the structural response of surrogate high burnup fuel rods to investigate the impacts of interfacial bonding efficiency at pellet-pellet and pellet-clad interfaces on spent nuclear fuel (SNF) vibration integrity. The FEA simulation results were validated and benchmarked with experimental measurements on surrogate rods consisting of stainless steel (SS) tubes with alumina-pellet inserts using Oak Ridge National Laboratory's (ORNL's) reverse bending fatigue test system.

A two-inch gauge section model of a surrogate fuel rod was used in the FEA development using the ABAQUS code. The FEA model consists of SS clad, alumina pellets, and an epoxy compliant layer that functions as a cohesive bonding media. Bending moments (M) are applied to the FEA models to evaluate the system responses of the surrogate rods. From the induced curvature κ, the flexural rigidity EI can be estimated as $EI = M/\kappa$.

Based on a series of FEA simulations, observations and conclusions concerning the impact of the interface bonding efficiency to SNF vibration integrity are provided in this report; this includes the moment carrying capacity distribution between pellets and clad, and the impact of cohesive bonding on the flexural rigidity of the surrogate rod system. As progressive de-bonding occurs at the pellet-pellet interfaces and at the pellet-clad interface, the load ratio of the bending moment carrying capacity gradually shifts from the pellets to the clad; the clad then starts to carry a significant portion of the bending moment resistance until reaching the full de-bonding state at the pellet-pellet interface regions. This results in localized plastic deformation of the clad at the pellet-pellet-clad interface region. The associated plastic deformations of the SS clad leads to a significant degradation in the stiffness of the surrogate rod. In one analysis, the flexural rigidity was reduced by 39% from the perfect bonding state to the de-bonded state at the pellet-pellet interfaces.

After de-bonding at the pellet-clad interfaces, the clad gradually assumes the majority of the bending moment resistance. This significant load shift leads to the clad yielding throughout the gauge section on the tension side of the sample, with a further reduction in the flexural rigidity of the surrogate rod system. On the compression side of the surrogate rod, the pellets are in direct contact to each other at the upper or bottom corners of the pellets. This enables the pellets to carry a large portion of the bending moment resistance, especially for the case of "no gaps" at the pellet-pellet interfaces. This in turn significantly reduces the intensity of the compressive stress field experienced by the clad under bending cycle fatigue, i.e., the surrogate rod will experience a full tension stress and less intensity in compression stress in the clad during the reverse bending fatigue cycles.

The immediate consequences of interface de-bonding are a shift in the load carrying capacity of the system from the fuel pellets to the clad, and the reduction of the composite rod system flexural rigidity. Therefore, the flexural rigidity of the surrogate rod and the bending moment resistance capacity between the clad and fuel pellets are strongly dependent on the interface bonding efficiency at the pellet-pellet and pellet-clad interfaces.

This page intentionally left blank.

TABLE OF CONTENTS

This page intentionally left blank.

LIST OF FIGURES

LIST OF TABLES

This page intentionally left blank.

USED FUEL DISPOSITION CAMPAIGN

FY 2014 STATUS REPORT: USING FINITE MODEL ANALYSIS AND OUT OF HOT CELL SURROGATE ROD TESTING TO ANALYZE HIGH BURNUP USED NUCLEAR FUEL MECHANICAL PROPERTIES

1. INTRODUCTION

1.1 Background

This research is being conducted in support the US Department of Energy (DOE) Used Fuel Disposition Campaign to develop computational modeling capabilities to support the understanding and interpretation of experimental test results, and to support the potential use of out of cell testing to extend the knowledge base of high burnup used nuclear fuel (UNF) material characteristics as the fuel experiences vibration due to the normal conditions of transport (NCT). This data has historically been developed using more expensive and time-consuming hot cell testing [1]. For high burn-up spent nuclear fuel (SNF), the fuel pellets and clad are normally fused together to form an integrated SNF system. To understand the underlying mechanism of the pellet-pellet and pellet-clad interface dynamics in a transportation environment it is essential to accurately evaluate the mechanical properties of the integrated SNF system. In concert with conducting physical experimentation on high burn-up SNF, Oak Ridge National Laboratory (ORNL) has developed a series of finite element analysis (FEA) protocols to investigate SNF vibration integrity using a surrogate rod system that resembles a SNF composite rod system.

It is important to identify, understand, and quantify the key mechanical properties of UNF as it experiences vibration during the expected NCT to a storage/disposal site. Recent out of cell and in cell testing have shown that the bonding efficiency at the pellet-pellet interface and at the pellet-clad interfaces of the high burn-up SNF system under normal transportation can have a significant effect on the fuel/clad system performance. ORNL has used FEA methods to develop simulation protocols, in addition to experimental calibration and verification efforts to establish the qualitative as well as the quantitative assessments of the SNF rod system performance during normal SNF transportation conditions. This report provides FEA and out of cell surrogate rod test information to support evaluation of the effects of pellet-pellet and pellet-clad interactions while considering the interfacial bonding efficiency on SNF vibration integrity. This methodology provides a solid road map for further FEA model development with respect to the effective fatigue life prediction of the SNF system under normal transportation vibration. The current methodology is focused on assessing the influence of interfacial bonding at the pellet-pellet and the pellet-clad interfaces to SNF vibration integrity.

The FEA models of a surrogate rod system is formed by alumina pellets and stainless steel tubing, with the appropriate boundary conditions, including the bonded epoxy at the clad/pellet interfaces. The model consists of a surrogate rod with 3D representation of fuel pellets, clad, and possible combinations of the gaps at the pellet-pellet and pellet-clad interfaces. The ABAQUS code was used in the FEA and the surrogate rod was represented by the beam element with the associated effective stiffness. This approach was used to obtain the effective properties of the beam elements that can be used as input for the further developments of the detailed SNF assembly model. The approach is also designed to estimate the damping properties of the beam elements due to frictional resistance between the clad and embedded pellets. This pellet-clad interaction modeling uses a "contact element" algorithm and can be further implemented into other embedded boundary conditions, such as internal pressure and residual stress, etc.

This study provides the detailed explanations on the effects of pellet-pellet and pellet-clad interactions, including pellet fracture and pellet-clad bonding efficiency, to the clad performance reliability under normal transportation considerations. The FEA simulation results were also calibrated and benchmarked with the fatigue aging data [2, 3] obtained from ORNL reverse bend fatigue testing.

1.2 Scope of Current Research

The objective of this research is to validate the pin models used in finite model analysis through investigation of the potential impact of interfacial bonding efficiency at pellet-pellet and pellet-clad interfaces and to understand how the bonding efficiency affects SNF vibration integrity. The FEA simulation results are validated and calibrated using ORNL reverse bend fatigue testing on surrogate stainless steel (SS) rods with alumina-pellet inserts.

The FEA models have a 2 in. gauge section that covers the SS clad and alumina pellets, as well as epoxy layers that serve as cohesive bonds. The models were developed using the ABAQUS code. In order to estimate the surrogate rod system responses including the stress profile and the associated curvature, κ, the bending moments (M) were applied to both ends of the surrogate rod. From the FEA results, the flexural rigidity (EI) of the simulation cases are estimated as, $EI = M/\kappa$. The detailed discussions of the simulation cases are divided into the following groups:

- the model with good interface bonding and without pellet fracture;
- the model with good bonding at pellet-clad interfaces and de-bonding at pellet-pellet interfaces; and
- the model with de-bonding both at pellet-clad and pellet-pellet interfaces.

The simulation results between pellets with flat end surfaces and pellets with chamfer in both ends will be compared and discussed as well. The simulation results indicate that the system response and the associated flexural rigidity are strongly dependent on the interface bonding efficiency.

2. INTERFACE BONDING EFFICIENCY ANALYSIS OF SURROGATE RODS

The structural analysis and interfacial bonding evaluation of surrogate rods used in the bending fatigue testing system [2-4] was carried out using the ABAQUS Code. ORNL developed a reverse bending fatigue testing system and used surrogate rods to calibrate and improve the test setup in an out-of-cell environment. In order to validate simulation results via out-of-cell surrogate data, the surrogate rod materials used in FEA are the same as that used in the out-of-cell testing. High density alumina was selected as the pellet material, and stainless steel (SS 304) was used as the clad material. Epoxy was used as the interface bonding material. The material properties of the surrogate rod are listed in Table 1.

2.1 Good Interface Bonding Without Rod System Fracture

Fig. 1 shows the geometry of a U-frame bending fatigue testing system with a co-planar configuration for the surrogate rod. The 2 in. gauge section is highlighted in black. A finite element model was developed to represent the 2 in. gauge section of the test specimen, referred to as the Clad-Epoxy-Pellet section model. Fig. 2 shows the cross section and longitudinal cut views of the 2 in. surrogate rod. The inside diameter (ID) and outside diameter (OD) of the clad are 0.382 in. and 0.436 in., respectively.

Table 1. Mechanical properties of surrogate rod

Material	Young's Modulus (psi)	Poisson's ratio	Yield strength (psi)	Density (lb/in.^{3})
Stainless Steel[a]	2.800E7	0.300	42061	0.2901
Al$_2$O$_3$[b,*]	5.395E7	0.22	3.626E5	0.1416
Epoxy[c]	5.076E5	0.37	10007.6	0.0452

[a][5], [b][6], [c][7, 8]

*The mean flexural strength of the purchased Al$_2$O$_3$ rod is 48 ksi provided by the vendor McMaster-Carr.

The alumina pellet OD is 0.372 in. Epoxy has a thickness of 0.005 in. In the first model, the alumina pellet was modeled with a 2 in. long alumina rod to simulate "a good interface bonding" at the pellet-pellet interface and without rod system fracture. Bending moments were applied on the both ends of the surrogate rod rotating along the X axis, as shown in Fig. 2 (b). According to the out-of-cell surrogate data, the bending moments ranged from 20N*m to 30N*m; the bending moment M_x was selected as 25N*m. Both loading surfaces of the surrogate rod were constrained with rotation along the Y and Z axes and translation along the X direction. In the following finite element models, the global mesh is 0.02 in. Some local meshes are as small as 0.0025 in.
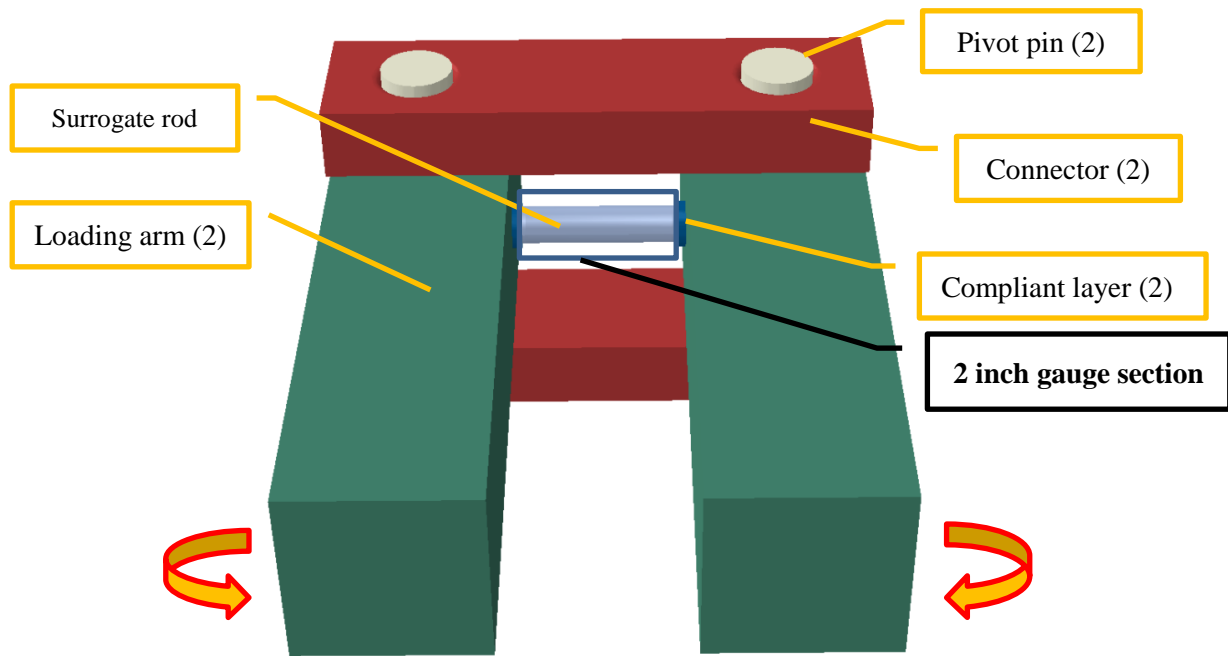
Fig. 1. Geometry of horizontal U-frame bending fatigue testing system with co-planar configuration of the rod.
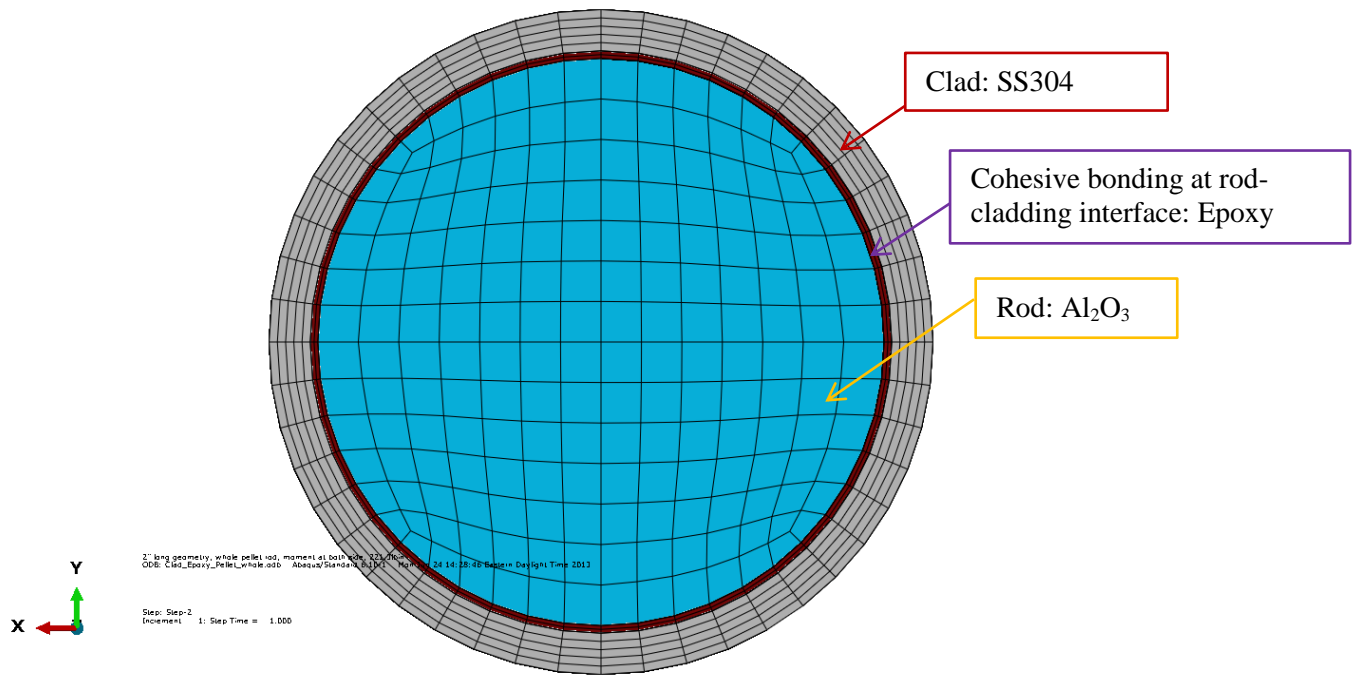
(a) Cross section view
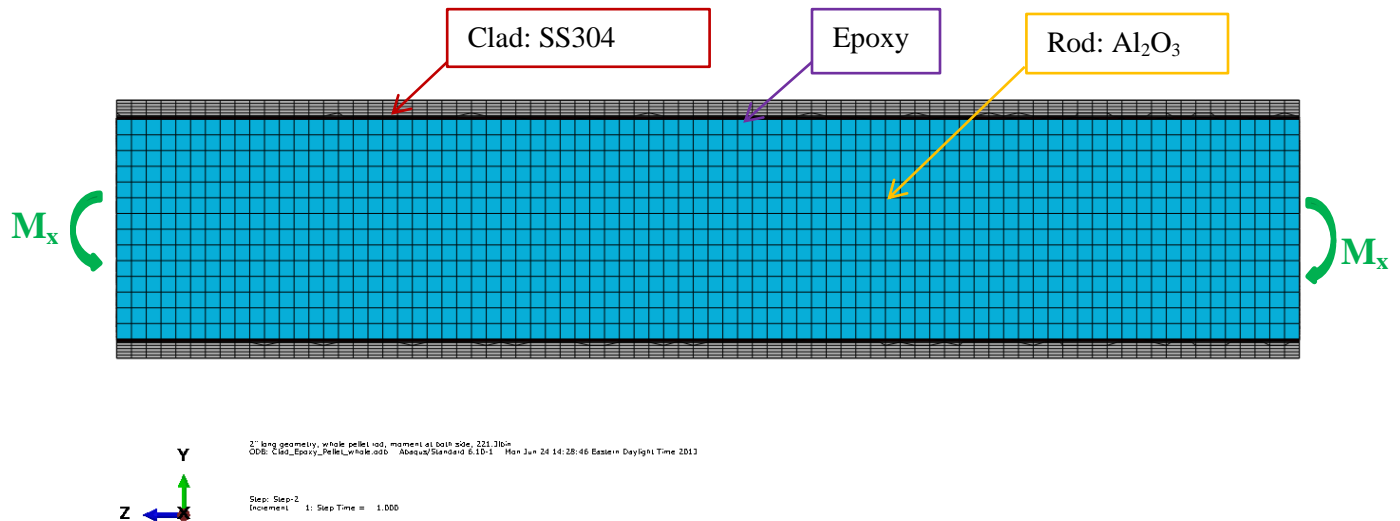
(b) Longitudinal cut view

Fig. 2. Geometry of Clad-Epoxy-Pellet section model with a single rod.

The quasi-static procedure is used in finite element analysis from the ABAQUS code. At the alumina rod-clad interface, thin epoxy layer elements are tied to both surfaces to simulate good cohesive bonds. The resultant stress distribution and curvature are shown in Fig. 3. The resultant curvature is 0.123 m^{-1}, too small to be noticeable, as illustrated in Fig. 3 (a). In order to see the bending effect, the curvature is deliberately enlarged 100 times in Fig. 3 (b). From the resultant stress distribution shown in Fig. 3, the maximum stress occurs at the outer surface of the alumina rod, and the resultant forces also indicate that the alumina rod carries a larger portion of the moment resistance than does the clad. The stress in the clad is under yield point of 42 ksi.
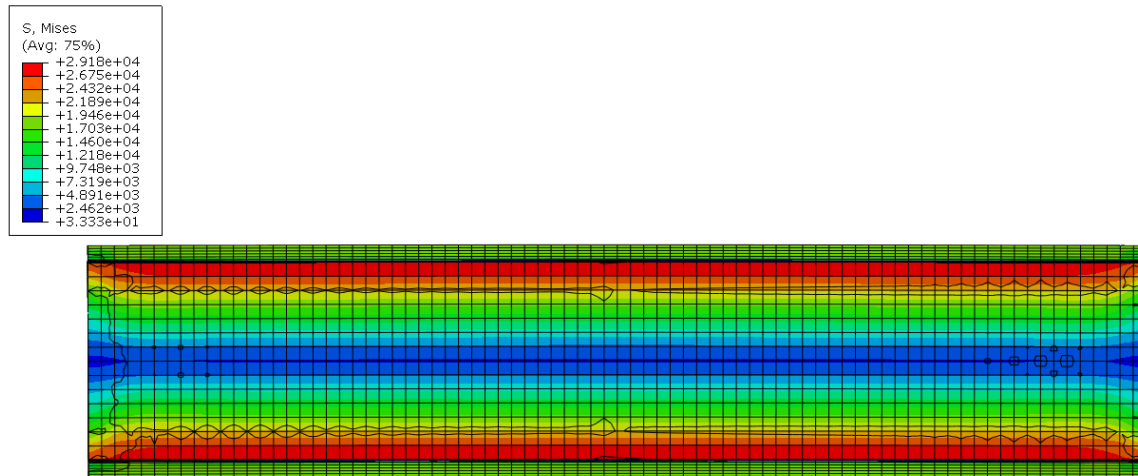
(a) Resultant curvature
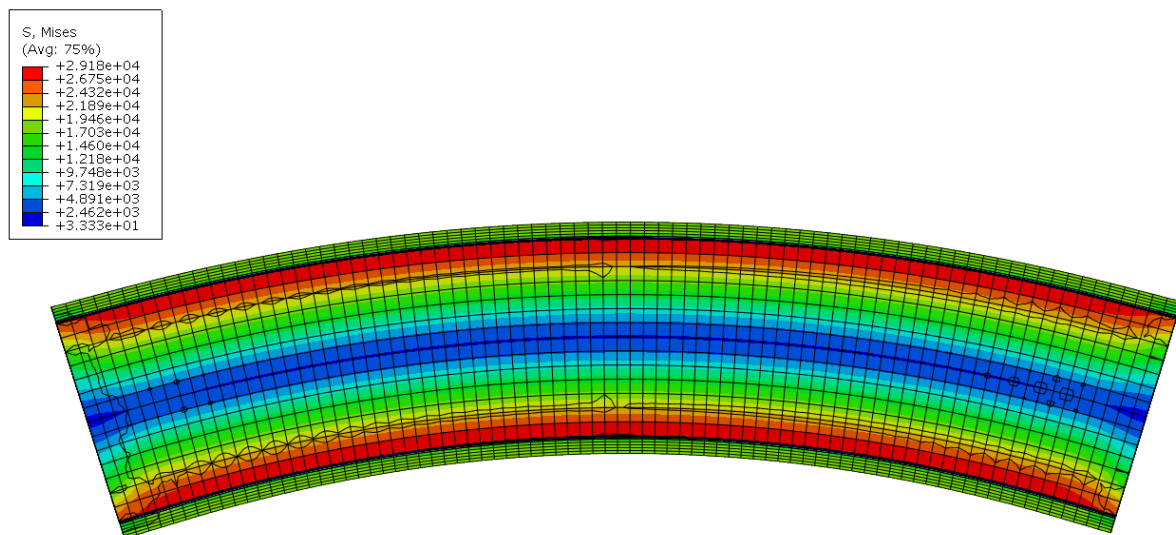
(b) Curvature increased 100x
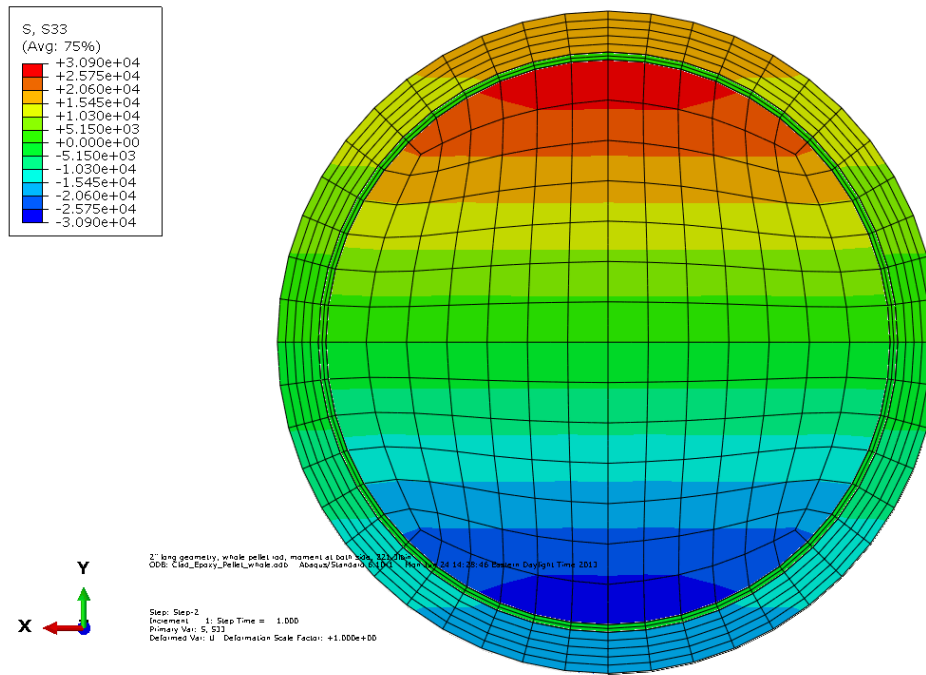
(c) Cross section view of resultant normal stress σ_{zz}

Fig. 3. Resultant normal stress distribution and curvature of Clad-Epoxy-Pellet section model with a single alumina rod insert.

The second model is the Clad-Epoxy-Pellet section model with four pellets and is shown in Fig. 4. This is similar to the Clad-Epoxy-Pellet section model with the single rod configuration. The materials and diameters of all components are the same as those used in the first model. The surrogate rod is 6 in. long and consists of 10 pellet inserts. Thus, each pellet is ~ 0.6 in. long regardless of the machining. Within the 2 in. gauge section, two pellets in the middle section have a full length of 0.6 in. and the two ends pellets have a partial length of 0.4 in. The boundary conditions of the surrogate rod are defined by having both ends clamped to simulate the rigid body motion associated with the loading arms of the reverse bend tester. Bending moments at both ends are set at 25N*m. This boundary condition is the same as the first model with a single rod insert.

In Fig. 4, the Clad-Epoxy-Pellet section model with four pellets, the configuration of the enlarged area is shown in Fig. 5. Pellets are modeled with round 0.002 in. end surfaces, and the end surfaces are flat. Thin epoxy layers are tied to the surfaces at the pellet-clad interfaces and at the pellet-pellet interfaces to simulate cohesive bonding. There are three 0.0014 in. gaps at the pellet-pellet interfaces filled with epoxy in this model. Loading and boundary conditions are the same as in the previous case.

(a) Cross section view   *(b) Longitudinal cut view*
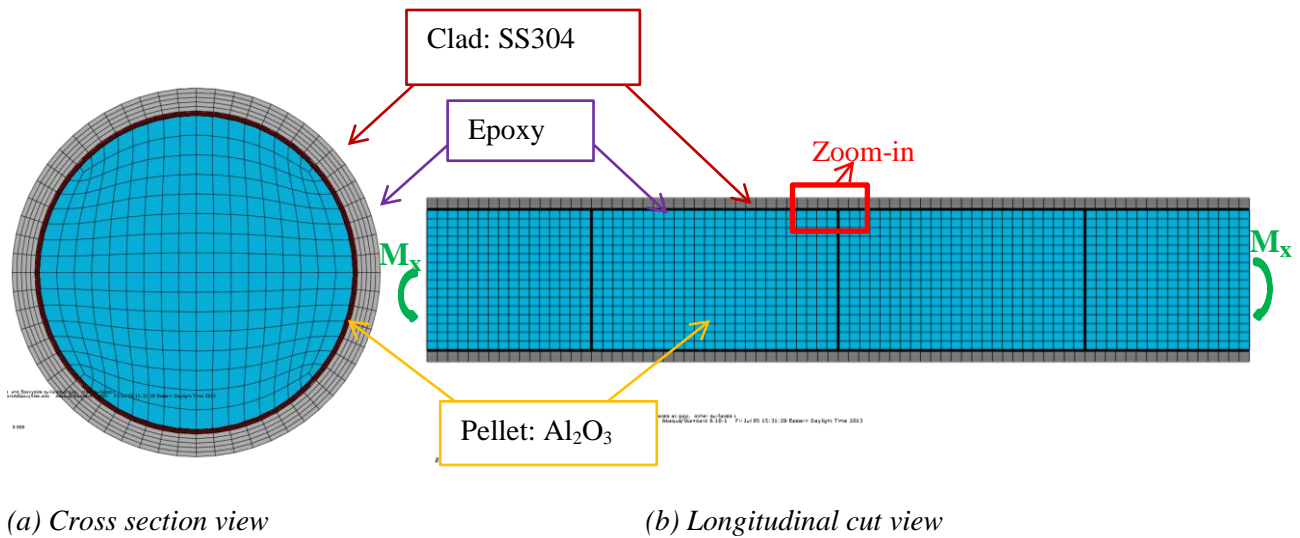
Fig. 4. Geometry of Clad-Epoxy-Pellet section model with four pellets.
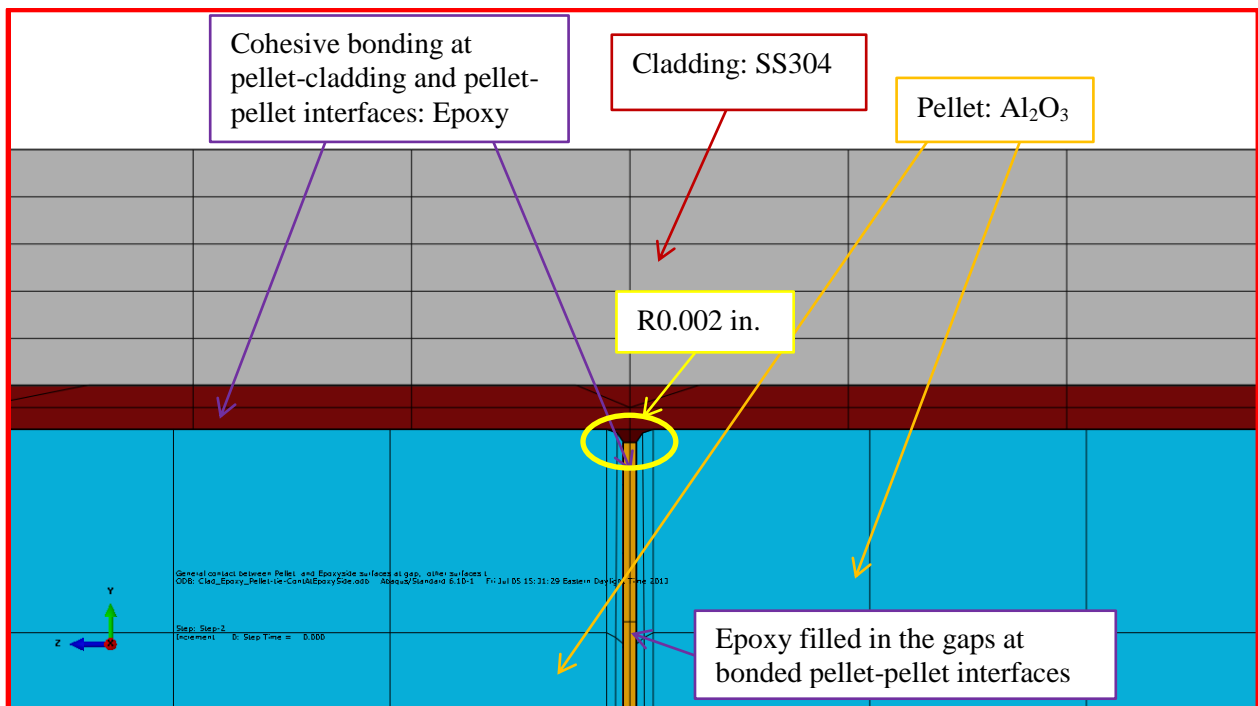
Fig. 5. Enlarged area in Fig. 4 for the case of epoxy filling in the gap at bonded pellet-pellet interfaces.

In Fig. 4, the Clad-Epoxy-Pellet section model with four pellets, the configuration of the enlarged area is shown in Fig. 5. Pellets are modeled with round 0.002 in. end surfaces, and the end surfaces are flat. Thin epoxy layers are tied to the surfaces at the pellet-clad interfaces and at the pellet-pellet interfaces to simulate cohesive bonding. There are three 0.0014 in. gaps at the pellet-pellet interfaces filled with epoxy in this model. Loading and boundary conditions are the same as in the previous case.

The stress distribution and curvature shown in Fig. 6 reveals similar results to that of the Clad-Epoxy-Pellet section model with a single rod. The resultant curvature is 0.141 m^{-1}. Maximum stress occurs at the outer surfaces of the pellets. Tied pellets carry most of the bending moment. The clad has not yielded under 25N*m bending moment, nor has the alumina pellet, which has a much higher yield strength than the SS clad. This indicates that the surrogate rod of a perfect bonding condition will remain within the linear elastic range under the target loading.
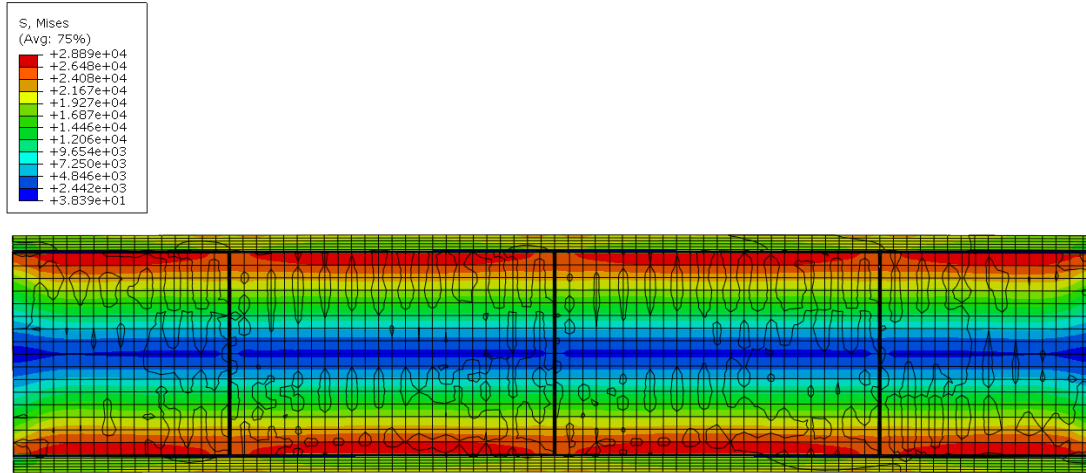
(a) Longitudinal cut view of resultant curvature and von Mises stress
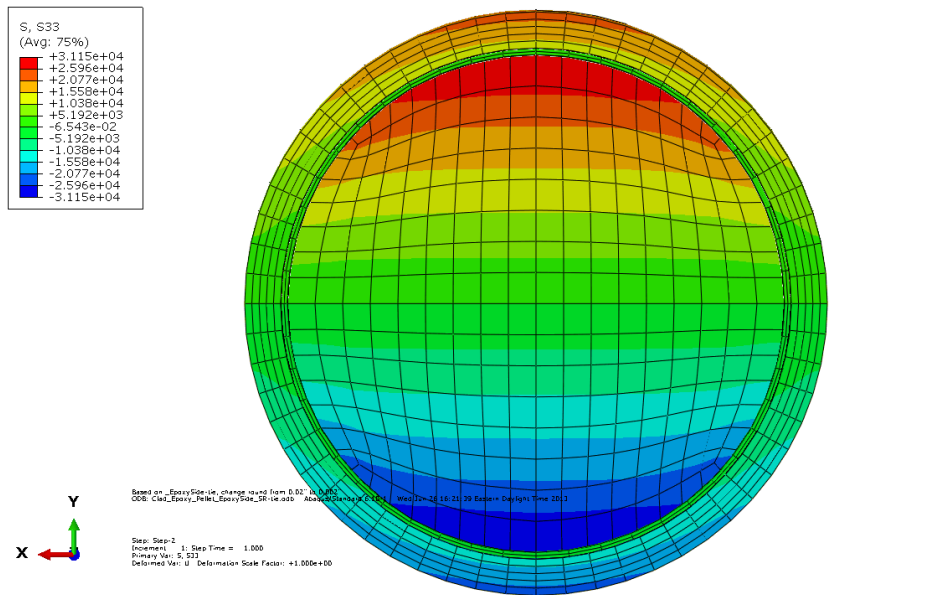
(b) Cross section view of resultant σ_{zz} at a pellet-pellet interface

Fig. 6. Resultant normal stress distribution and curvature of Clad-Epoxy-Pellet section model of four flat pellets and epoxy filling in gaps at pellet-pellet interfaces.

Fig. 7. AREVA Front End Business Group designed fuel pellet for nuclear reactors.

In modern fuel, the fuel pellets are manufactured with dip and chamfer on the end surfaces to reduce pellet surface clinging or the potential for a bambooing effect, as shown in Fig. 7. Therefore, the surrogate fuel pellets were modeled with dip and chamfer on the end surfaces of the pellets to investigate how this condition may affect the associated bonding efficiency. Fig. 8 shows both ends of a fuel pellet constructed with a dip of diameter 0.28in. and depth 0.01 in.; and the round edge of the end surfaces is increased to 0.02 in., 10 times that of the previous model in Fig. 5.

Fig. 8. Surrogate fuel pellet model with dips in both ends.
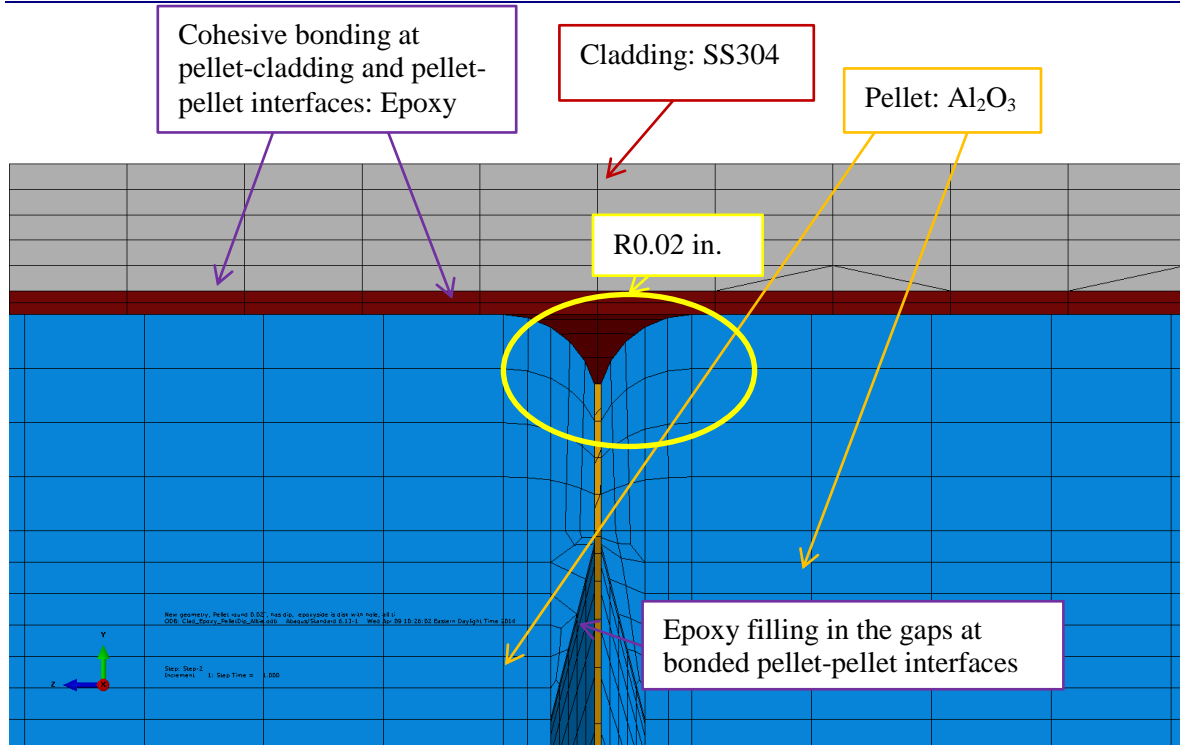
Fig. 9. Enlarged area from Fig. 4 for the case of epoxy filling in the gap at the bonded pellet-pellet interfaces, pellets with dips and round 0.02in.

Fig. 9 shows the assembly of surrogate fuel pellets and cladding in the enlarged area. The material and components of the section model remain the same. Thin epoxy layers are tied to the surfaces at the pellet-clad interfaces and at the pellet-pellet interfaces to simulate cohesive bonding. Loading and boundary conditions are the same as in the previous cases. However, the differences are the dips in pellet ends and the bigger round ends on the pellet end surfaces.

Fig. 10 illustrates the results of stress distribution and curvature of the section model for pellets with dips and with epoxy tied to both pellet-clad and pellet-pellet interfaces. The stress distribution appears to be different from those of the previous two models. Instead of maximum stress distributing along the pellets, the maximum stresses concentrate on the limited tie areas. This occurs because of the dips in the end of the pellets cause contact surface to be limited. Perfect bonding assigned to the interface tie area are carrying most of the bending moment resistance. The maximum stress level is higher than that observed in the cases where the fuel rod and fuel pellets were without dips. However, maximum stress is seen at the pellet tie area, as shown in σ_{zz} of Fig. 10 (c). The maximum stresses of the clad and pellets are all under yielding strength, thus, the surrogate rod under the target load is still in the linear elastic region. The curvature for this case is 0.158 m^{-1}.
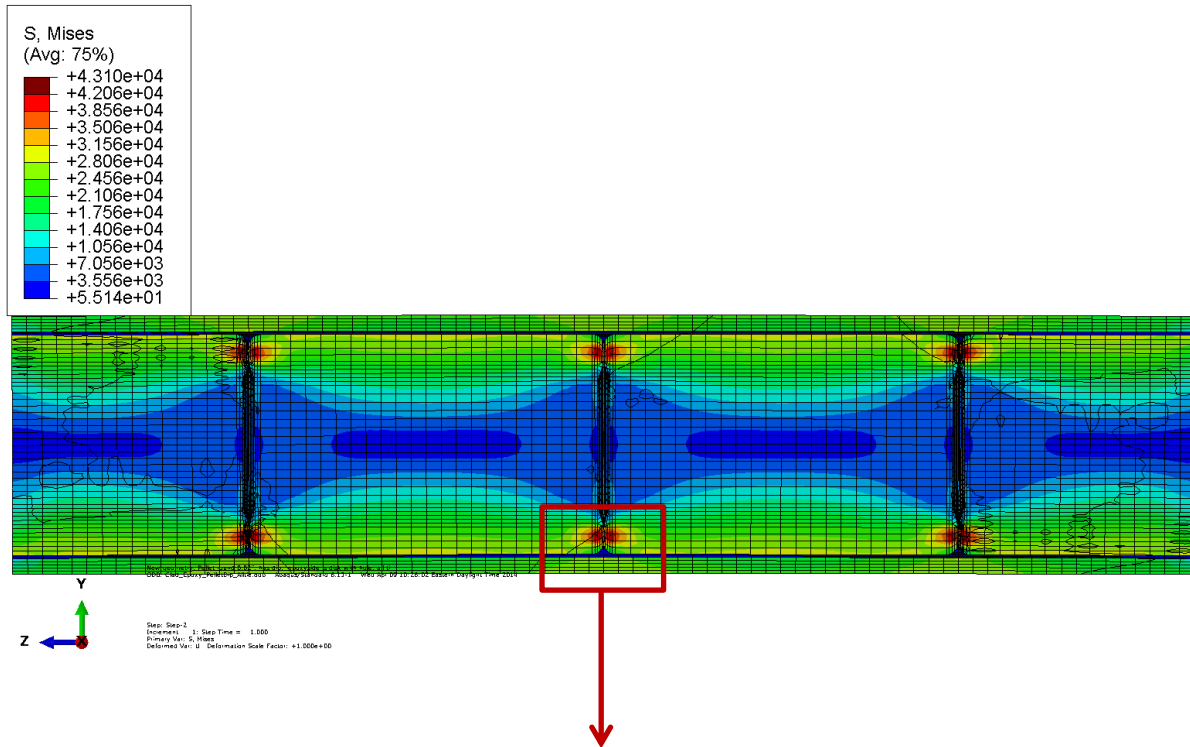
(a) Longitudinal cut view of resultant curvature and von Mises stress
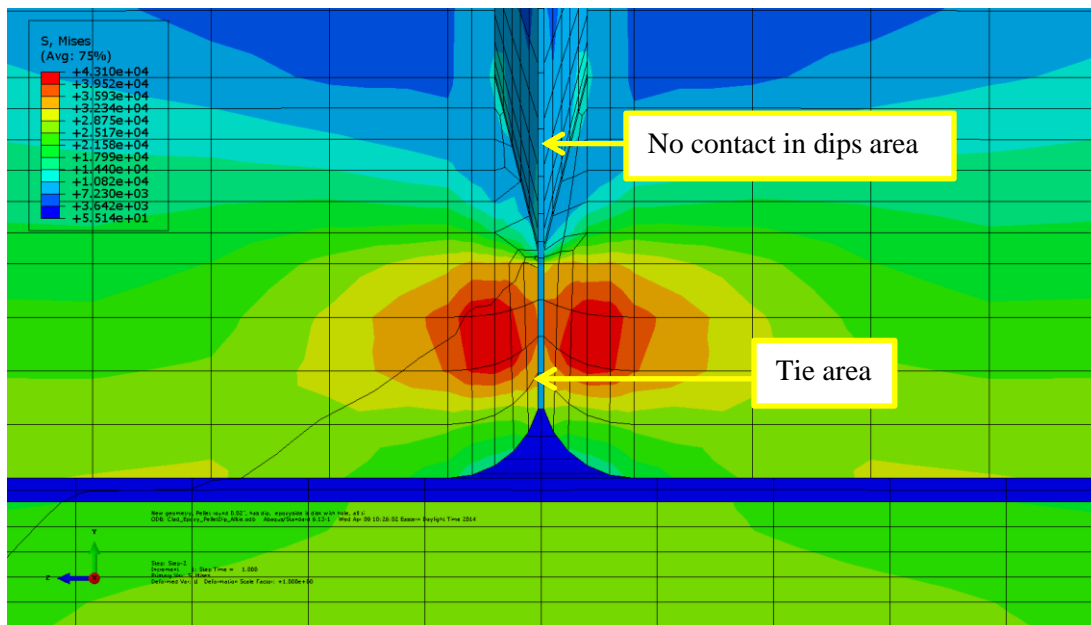
(b) Detailed view in the enlarged area

(c) Cross section view of resultant σ_{zz} at a pellet-pellet interface

Fig. 10. Normal stress distribution and curvature of Clad-Epoxy-Pellet section model of our pellets with dips and epoxy filled gaps at the pellet-pellet interfaces.

Symmetrical reverse output force was obtained for a composite rod (SS tube + single alumina rod) using U-frame bending fatigue testing system (CIRFT), as shown in Fig. 11. Displacement control was used for bending tests with amplitudes of 0.118 in. to 0.512 in. (3–13mm), frequency of 0.1 Hz, and the deflection was measured at the mid-point of the rod. The composite rod bending test results indicate that before alumina rod fracture, the composite rod responded linearly and most of the bending load carrying capacity resided on the alumina rod due to the rod having twice the Young's Modulus compared to that of SS clad. When the alumina insert fractured, a sudden load transfer then occurs and SS tube starts to carry the majority of bending moment. This situation results in plastic deformation of SS clad, which is discussed in the following simulation cases.

Three simulation cases using a surrogate rod with good interface bonding and without rod fracture were studied. In order to simulate a good cohesive bonding in FEA, the interfaces of the pellet-clad are tied with a thin epoxy layer, while the pellet-pellet interfaces are either modeled as a single rod or tied with epoxy filling in the gaps.
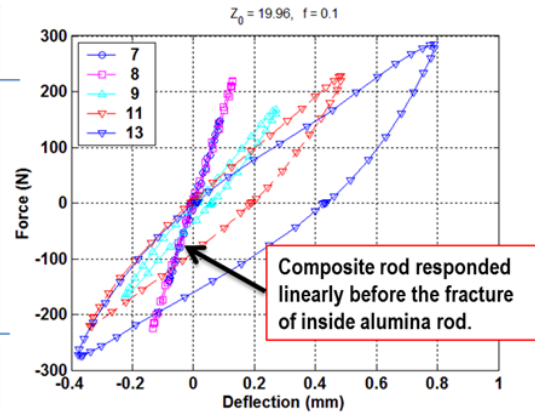
Fig. 11. Symmetrical reverse output force obtained for composite rod (SS tub + alumina rod) using the CIRFT system with a displacement input: 0.1 Hz, amplitude 0.118 in. to 0.512 in. [2, 3].

The curvature and flexure rigidity for these cases are summarized in Table 2. In this analysis, a load control procedure was used, and the bending moment M was applied to both ends of the surrogate rod. The bending curvature κ is estimated from FEA results within the gage section. The flexural rigidity EI (the product of Young's Modulus E and moment of inertia I) of a surrogate rod can be estimated using the applied moment M and the resultant curvature, κ, as described in Eq. 1.

$$EI = M/\kappa \tag{1}$$

Table 2. The curvature and flexural rigidity for the perfect interface bonding simulation

	Curvature κ (1/m)	Bending moment M (N*m)	Flexural rigidity EI (N*m^2)
Clad-Epoxy-Rod-Tie	0.123	25	203
Clad-Epoxy-Pellet (4)-Tie-Pellet-Tie-at Gap	0.134	25	186
Clad-Epoxy-Pellet (4) -Tie-Pellet with Dip - Epoxy-Tie-at Gap	0.158	25	158

Table 2 shows that the flexure rigidity variations are due to interface bonding and the interface geometry. Pellet-pellet interfaces tied together results in 8% curvature increase compared to that of the single rod case. Pellet-pellet interfaces where epoxy filled in the gaps from the dips and larger round end surfaces further increased curvature by up to 24% compared to that of the single rod case. The ORNL surrogate rod testing specimens is more closely resembled to the third case, i.e., Clad-Epoxy-Pellet section model with four pellets where epoxy filled in gaps at all pellet-pellet interfaces. In one test, alumina pellets were bonded to the SS tube and to each other using epoxy. The specimen was tested under a 25N*m bending moment. High flexural rigidity was observed, as shown in Fig. 12. The initial (first cycle) test data, which has highest flexural rigidity indicates that the pellet-clad and pellet-pellet interface bonds should remain intact. Flexural rigidity of the first test data is very close to the FEA estimation of 158N*m^2.

With good interface bonding and without alumina rod fracture, the alumina rod can carry a significant bending moment under normal transportation vibration due to it having twice the Young's Modulus compared to that of the SS clad, in addition to exhibiting a much higher compressive strength, as shown in Table 1. Mechanical properties of surrogate rod Surrogated data validates that pellets can carry more

moment resistance than the clad due to its higher stiffness as long as the pellet-clad and pellet-pellet interface bonds remain intact. Before the alumina rod fractured, the rod responds to the bending moment within the linear elastic range. The high flexural rigidity estimated from FEA is in good agreement with that estimated from bending fatigue testing data. Furthermore, under cyclic loading it is expected that the interface bond will be progressively degraded, as demonstrated in Fig. 10 with decreasing flexural rigidity under increased loading cycles.
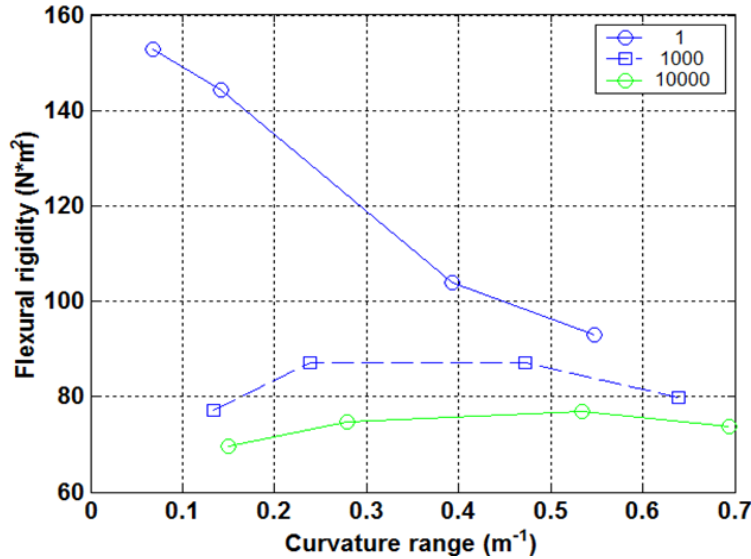

Fig. 12. Specimen test data, flexural rigidity vs. curvature [3].

2.2 The Effect of Pellet-Clad Interface Bonding Efficiency

There are inherited stress fields in the SNF system, including axial tensile stress and tangential tensile stress due to pellet-clad mechanical interaction, and oxide volume expansion, radial compressive stresses due to hydride compaction, and tangential shear stress due to hydride volume expansion. Vibration during transportation will induce reverse bending in a SNF assembly. Repeated expansion and contraction in both axial and tangential directions of the SNF rod due to reverse bending flexural deformation, combined with stress concentrations, can degrade the interface bonding at the fuel pellet-clad interfaces and pellet-pellet interfaces, as shown in Fig. 13. While the shear stress is small relative to the normal stress due to bending, it cannot be neglected. In particular, in a composite rod or in SNF rods, excessive shear due to material mismatch can be a cause for interface bonding failure.

At pellet-pellet interfaces, the interface bonding failure is mostly caused by the normal stress due to reverse bending flexural deformation, combined with relatively smaller shear stress (Fig. 13). At pellet-clad interfaces the localized high shear stress will also increase due to the material mismatch under flexural deformation. Because the shear stress is small relative to the normal stress, it is likely that the interfacial bonding failure at pellet-pellet interfaces will initiate before the de-bonding at pellet-clad interfaces. Observation from ORNL CIRFT testing on surrogate SS rods with alumina pellets verified this hypothesis.

The Clad-Epoxy-Pellet section model with four pellets was used to investigate the surrogate rod bending response with perfect bond at pellet-clad interface and de-bond state at pellet-pellet interface. The material properties, geometry, and loading and boundary conditions are the same as that used in the previous FEA simulation.

(a) Bending flexural strain field

(b) Axial compression stress fields
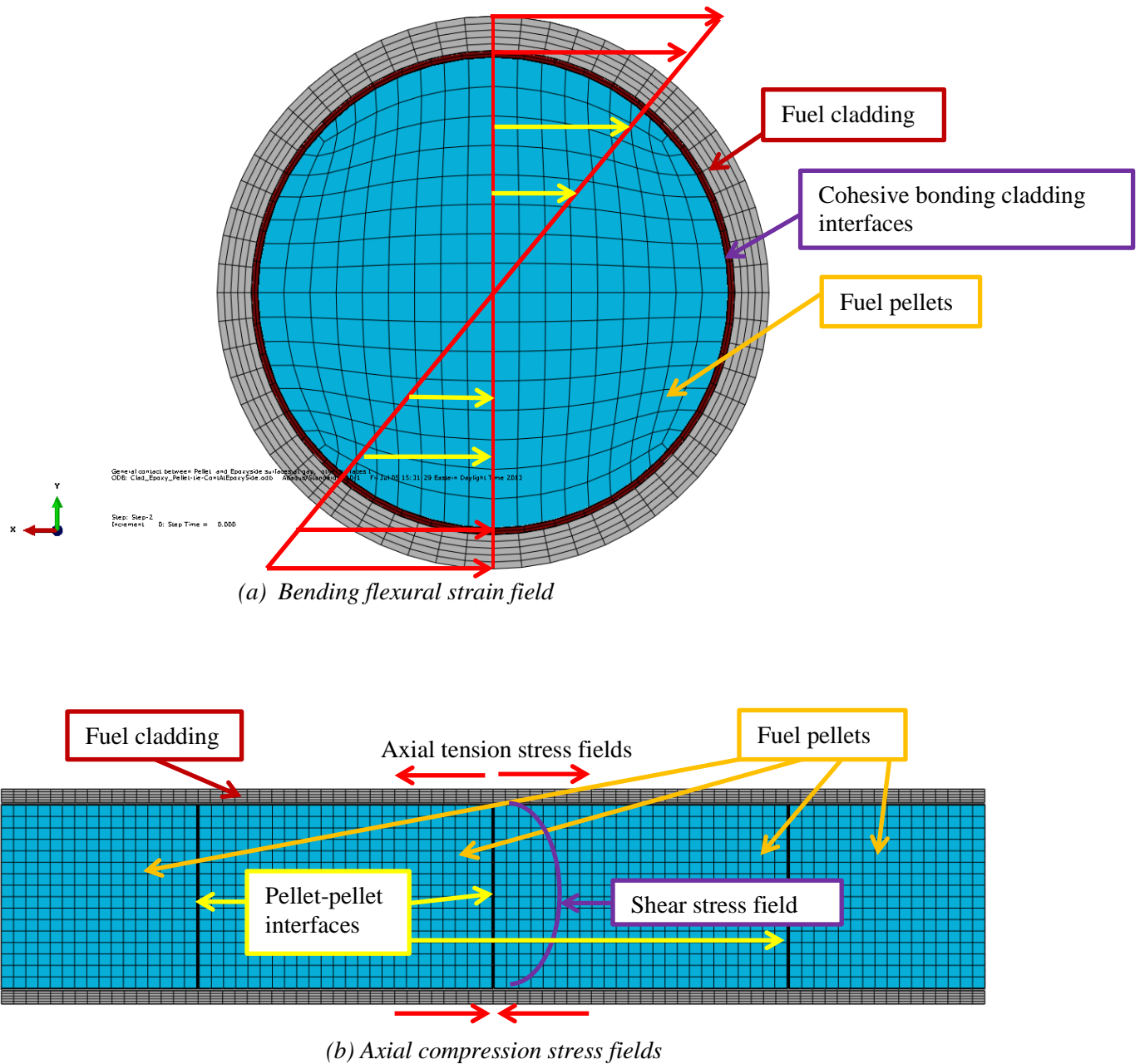
Fig. 13. Transportation induced reverse bending stress fields in a SNF system.

To simulate a good cohesive bond condition at the pellet-clad interfaces, a thin epoxy layer was tied to the pellet-clad interfaces surfaces. The first case study was designated to simulate the response with de-bonded pellet-pellet interfaces. Pellet-pellet interfacial de-bonding was defined as no epoxy or gaps at the pellet-pellet interfaces (Fig. 14). Pellets have no dish and do have flat end surfaces with round 0.002 in.
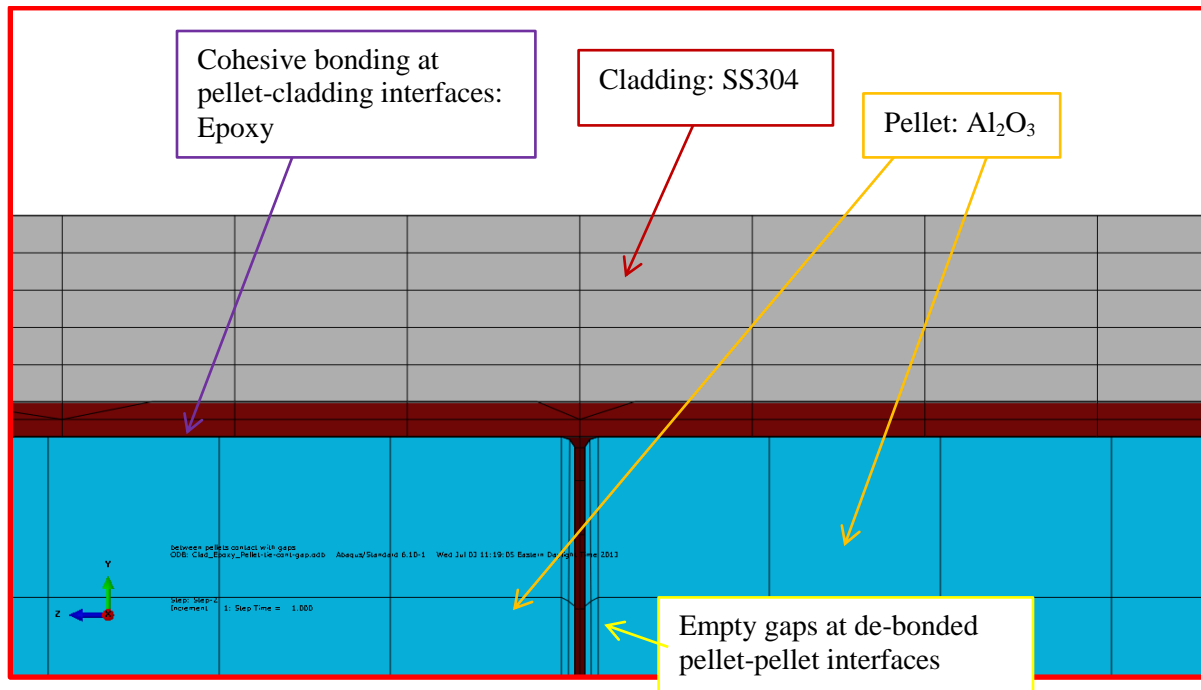
Fig. 14. Enlarged area in Fig. 4 for the case of empty gaps at de-bonded pellet-pellet interfaces.

The stress and curvature responding to the bending moment are illustrated in Fig. 15. Compared to the results shown in Fig. 6, there are significant differences in the stress distribution between the pellet-pellet interface bond case and the pellet-pellet interface de-bond case, where the pellet-clad interface remains perfect bond for both cases. In pellet-pellet interface for the de-bonded case, the maximum tensile stress, which reaches the clad yield strength of 42 ksi, occurs at the clad and is located at the top and bottom portion of the pellet-pellet interface regions. In those areas of the tube with a perfect pellet-clad bond, the SS tube did not yield. The curvature profile with a ten-fold expansion shown in Fig. 15 (b) also shows a lateral contraction and lateral expansion at the tension and compression sides of clad. Furthermore, the localized clad buckle was also observed and is likely due to the lack of internal support at the pellet-pellet-clad interface gap region. The clad deforms continuously until the gaps are diminished by direct contact with the pellet-pellet surfaces. There are no stress concentrations observed at pellet-pellet contact corners. Resultant σ_{zz} clearly indicates that the clad takes over more bending moment resistance than that of the pellets at the de-bonded pellet-pellet interfaces.

At the de-bonded pellet-pellet interfaces, the pellets can only transfer load via hard contact, so the load carrying capacity shifts significantly from the pellets to the clad. When the SS tube starts to carry the majority of the bending moment at the pellet-pellet interface region, this results in a significant localized plastic deformation of the SS clad. In most of the gauge section, pellets continue to provide sufficient internal support to the clad due to good cohesive bonding at the pellet-clad interfaces, and carry most bending load. Therefore, there is no yielding in most regions of the SS clad.

The results of the perfect bond case (Fig. 6), shows that the pellets carry significant bending moment resistance. The maximum stress resides at the pellets and there is no yielding at either the pellets or the clad. It is interesting to note that the von Mises stress distribution in the de-bond pellets case appears to be in a dog bone shape due to contact pressure at the pellet-pellet interfaces. This is different compared with the results of the bonded pellet-pellet interface case. Another change lies in the induced curvature. In the de-bonded case the resultant curvature is 0.616 m^{-1}, which is more than 4 times of that of the perfect bond case shown in Fig. 6.
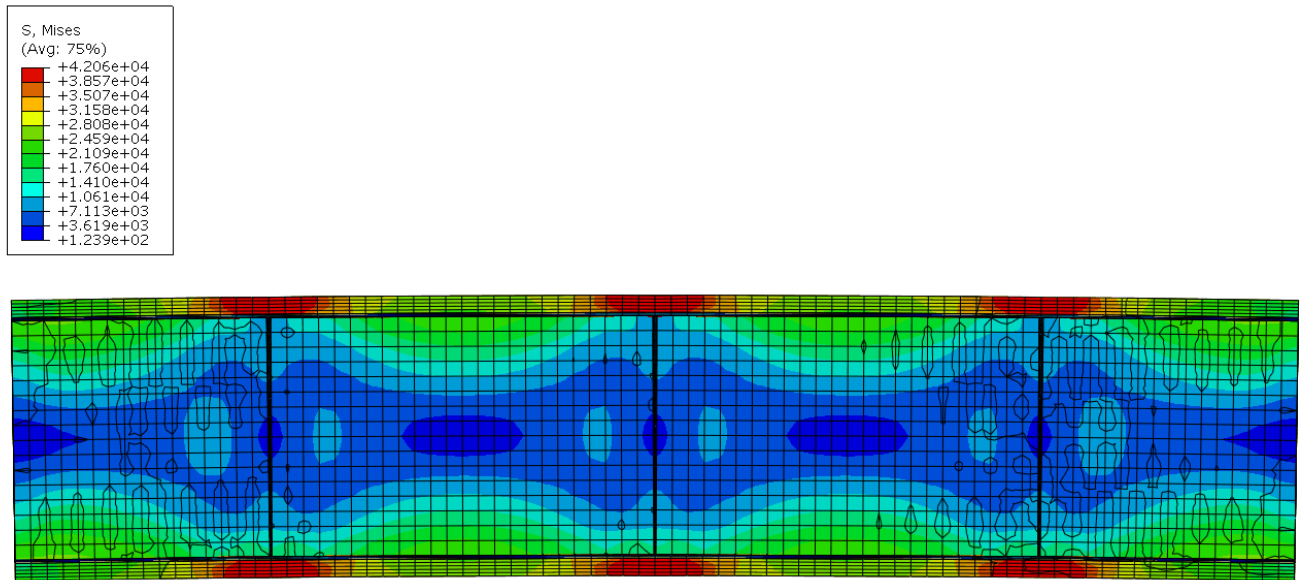
(a) Longitudinal cut view of resultant curvature and von Mises stress
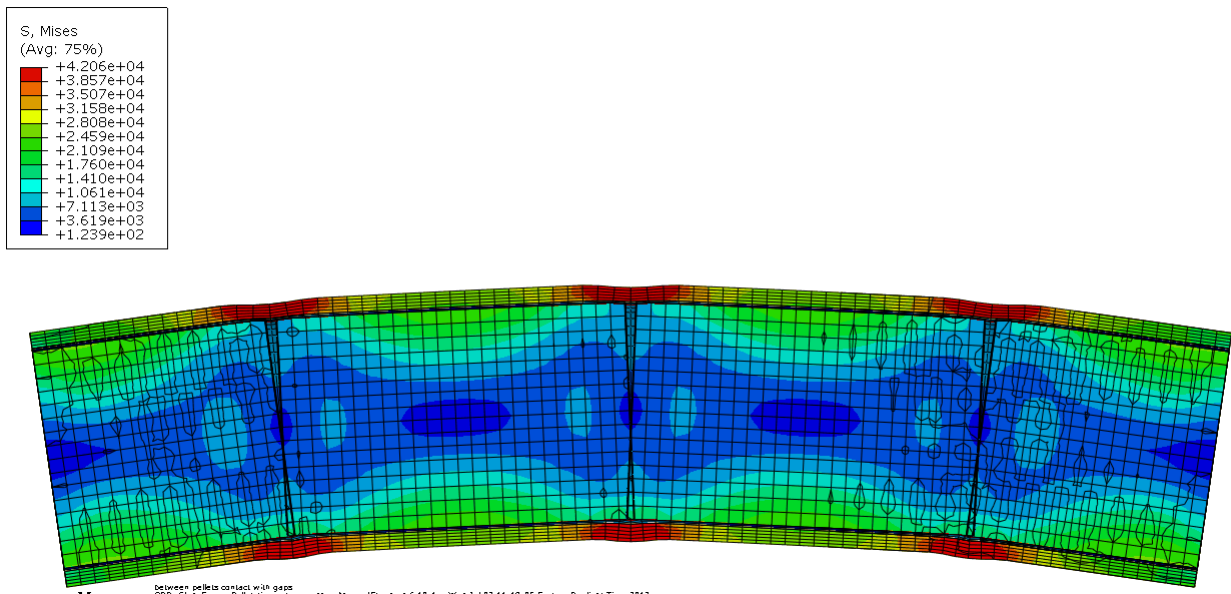
(b) Longitudinal cut view with curvature enlarged (10x)
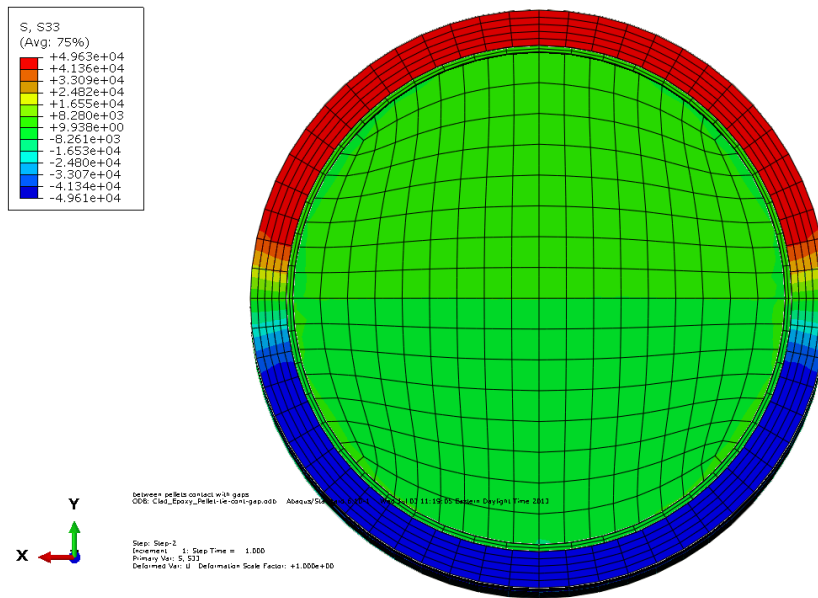
(c) Cross section view of resultant σ$_{zz}$ at a pellet-pellet interface

Fig. 15. Stress distribution and curvature of Clad-Epoxy-Pellet section model of four flat pellets with empty gaps at de-bonded pellet-pellet interfaces.

The second case study simulating pellet-pellet interfacial de-bonding was defined as having gaps at the pellet-pellet interfaces, while a thin epoxy layer still existed at the pellet-clad interfaces and tied then to the adjacent surfaces to provide perfect cohesive bonding. The pellets are modeled with dish on the ends and round fillet of 0.02 in. at the end surfaces. Fig. 16 shows the simulation results of the case with pellet-pellet interface de-bonding condition. This shows a very similar stress profile as that of Fig. 15, and the maximum stress occurs at the top and bottom portion of the clad region due to a significant load shifting to the clad. The majority of the SS tube did not yield due to the perfect pellet-clad bond. The cross section view of the resultant σ$_{zz}$ shows that the maximum compressive stress fields reside in the clad regions. No obvious stress concentration was observed at the pellets. Pellets have the same dog-bone shaped stress distribution as that of the previous case. The induced curvature of this pellet-pellet interface de-bonding with dish example is 0.620 m^{-1}, which is very close to what was observed in the previous pellet-pellet interface de-bonding case. The similarity between the flat pellet and the pellet with dish cases occurs because of de-bonding of the pellet-pellet interfaces and gaps between the pellets. Until the pellet to pellet interface gaps are closed, the clad is the primary material taking the bending load. Thus, the impact of pellet dish is minimized.
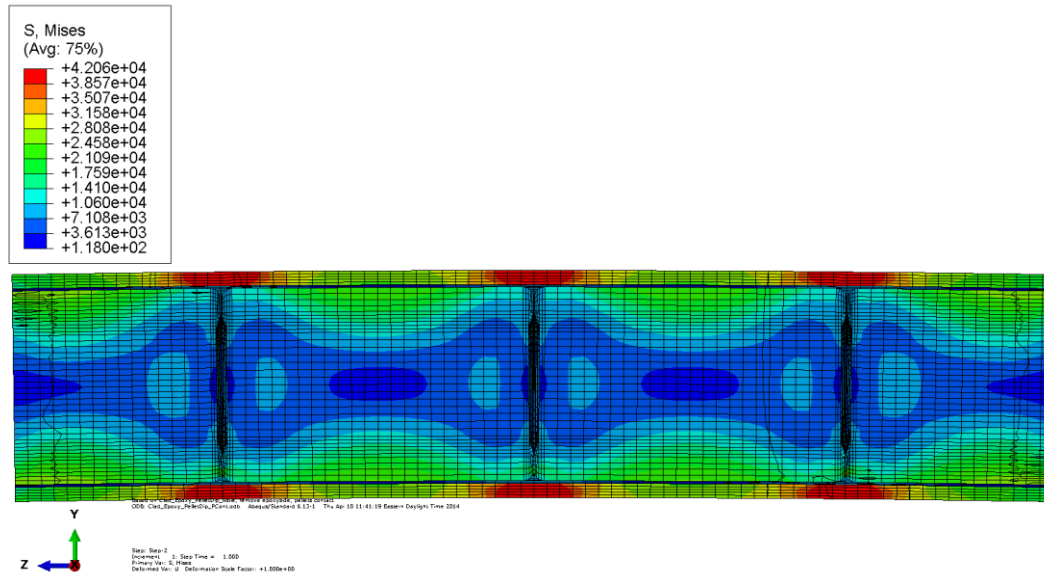
(a) Longitudinal cut view of resultant curvature and von Mises stress
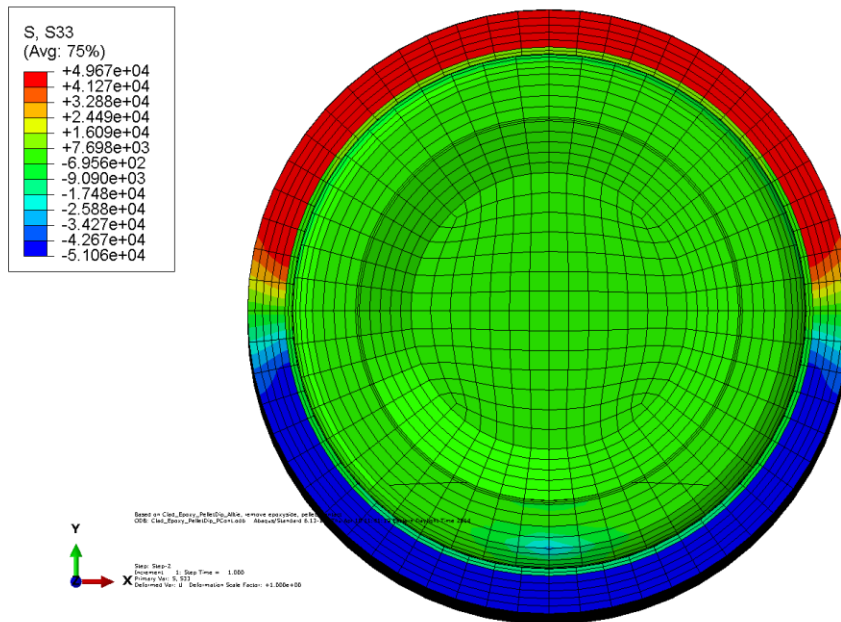
(c) Cross section view of resultant σ_{zz} at a pellet-pellet interface

Fig. 16. Stress distribution and curvature of Clad-Epoxy-Pellet section model of four pellets with dish and with empty gaps at de-bonded pellet-pellet interfaces.
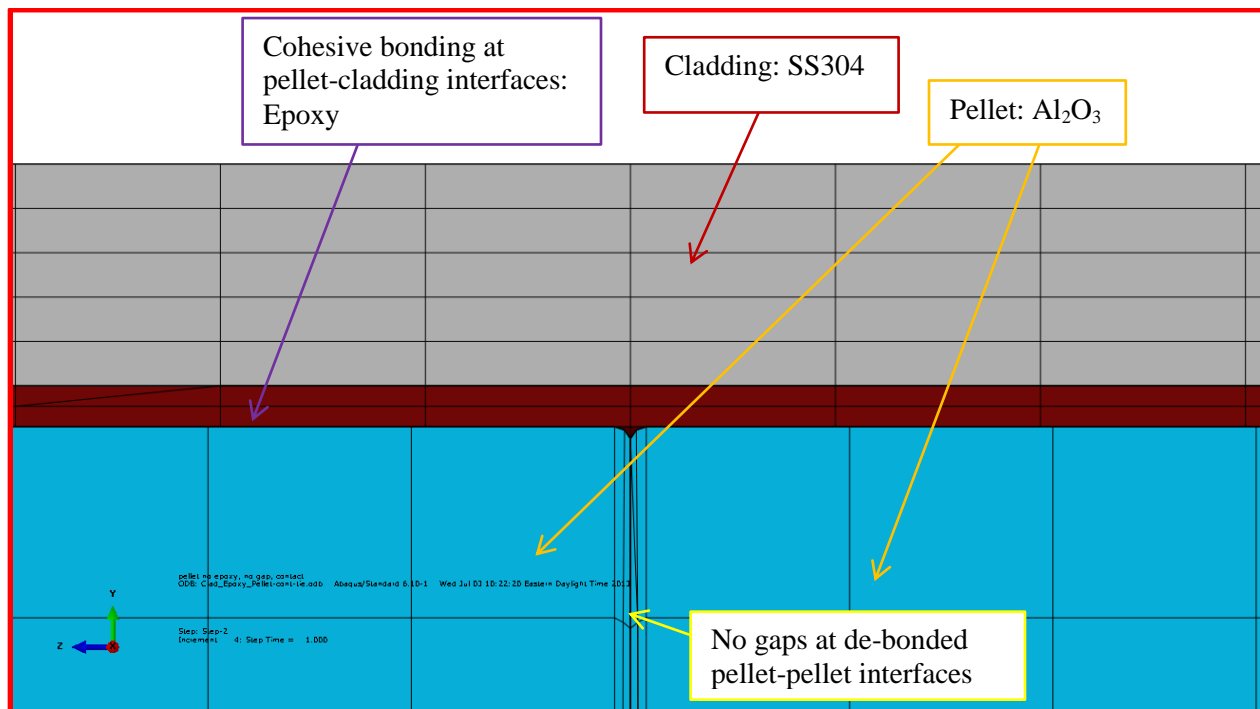
Fig. 17. Enlarged area in Fig. 4 for the case of no gaps at de-bonded pellet-pellet interfaces.

The simulation with "de-bonded pellet-pellet interfaces" and "bonded pellet-clad interfaces" is illustrated in Fig. 17. There are no gaps existing at the pellet-pellet interfaces before applying bending loads. Similar to the previous cases, a thin epoxy layer is applied and tied to surfaces at pellet-clad interfaces to simulate good cohesive bonding. In this case, pellet end surfaces are flat with round fillets of 0.002 in.
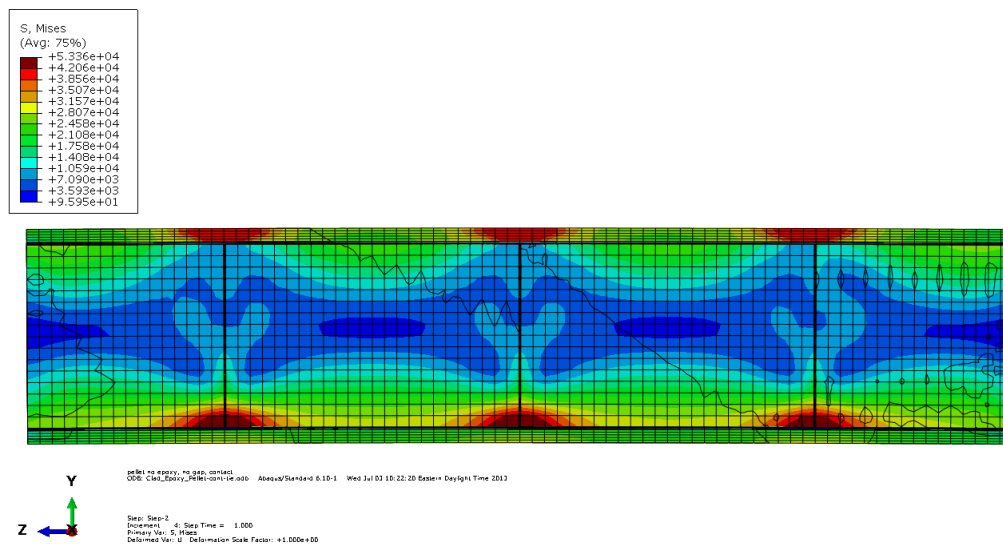
(a) Longitudinal cut view of resultant curvature and von Mises stress
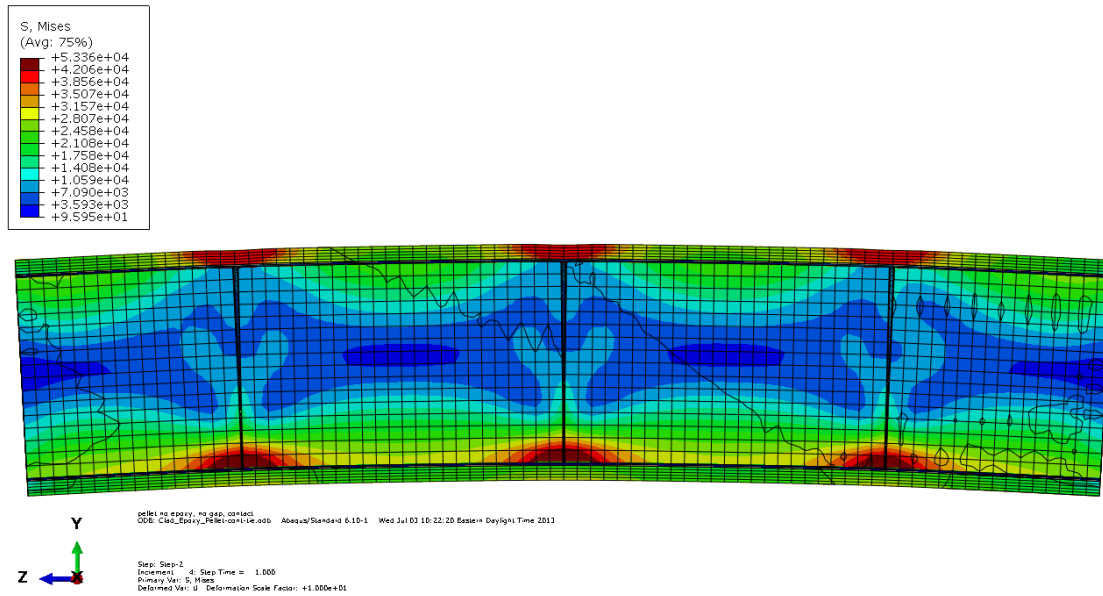
(b) Longitudinal cut view of curvature increased 10x
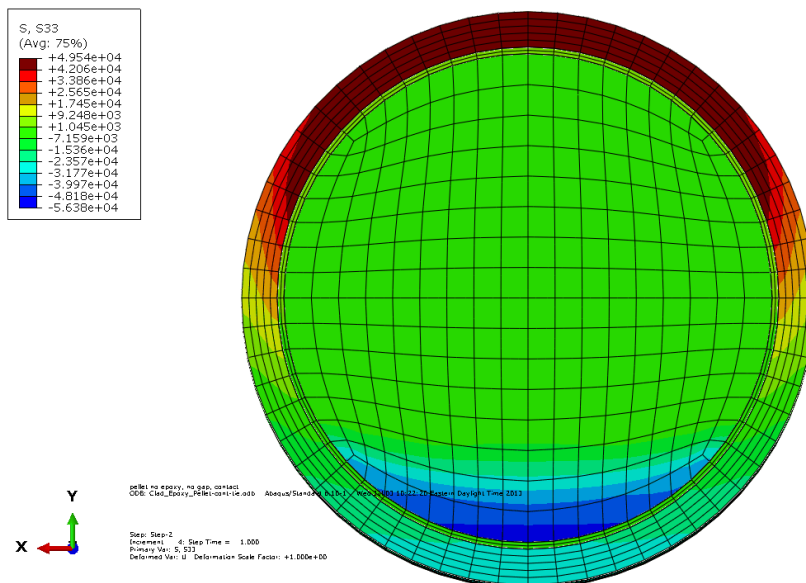
(c) Cross section view of resultant σ_{zz} at a pellet-pellet interface

Fig. 18. Stress distribution and curvature of Clad-Epoxy-Pellet section model of four flat pellets without gaps at de-bonded pellet-pellet interfaces.

As illustrated in Fig. 18, the stress distribution of this case simulation appears to be different from that of the de-bonded pellet-pellet interface case with gaps shown in Fig. 15. The SS clad reached its yield point at the top of the pellet-pellet interface regions. On the compression side interface the maximum stress occurs at the pellets instead of clad. Due to high compressive strength of the pellet, the pellet is in the

linear elastic range at the maximum stress level. From the curvature profile, there is no clad buckling observed at the bottom (compression) region. This is because there are no gaps at pellet-pellet-clad interface region. Thus, the pellets provide good internal support to the clad tubing structure. Furthermore, the pellets seem to carry a significant portion of the bending moment resistance via pellet-pellet interaction (pinching at the pellet corners), which significantly mitigates the stress level of the clad in the bottom (compression) region. The pellets stress profiles also show a dog-bone shape due to contact pressure at the pellet-pellet interfaces. The resultant σ_{zz} profile without gaps at the pellet-pellet interface indicates that the pellets can carry more bending moment resistance than that of pellets with gaps as shown in Fig. 15.

The fourth case in this section is similar to the third case, in that the simulation uses de-bonded pellet-pellet interfaces without gaps between the interfaces. The difference between simulations is the pellets with dish on the both ends and round fillets 0.02 in. at the end surfaces. Fig. 19 shows the resultant stress distribution and curvature of this simulation. The stress distribution generally is similar to that of the previous case shown in Fig. 18. Maximum stress also occurs at the pellets. However, the stress level is much higher than that shown in Fig. 18. From the detailed view in the expanded area, we can see that due to large round corners and no contact in the dish area, the pinching focused on the small contact area, resulting high contact stress levels. The resultant σ_{zz} shows the maximum stress on the pellet contact surface.

(a) Longitudinal view of curvature and von Mises stress

(b) Detailed view enlarged area
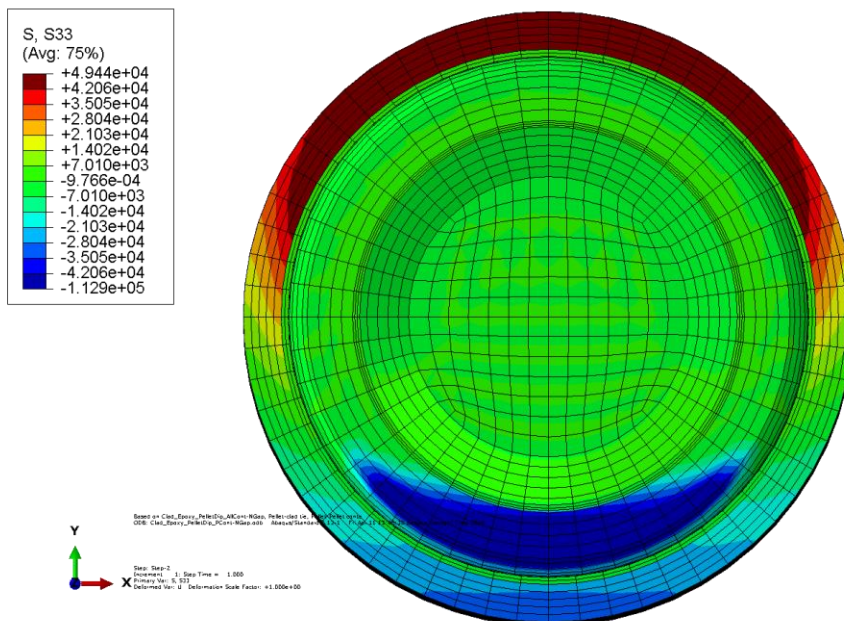
(c) Cross section view of resultant σ_{zz} at a pellet-pellet interface

Fig. 19. Stress distribution and curvature of Clad-Epoxy-Pellet section model of four pellets with dish and with no gaps at de-bonded pellet-pellet interfaces.

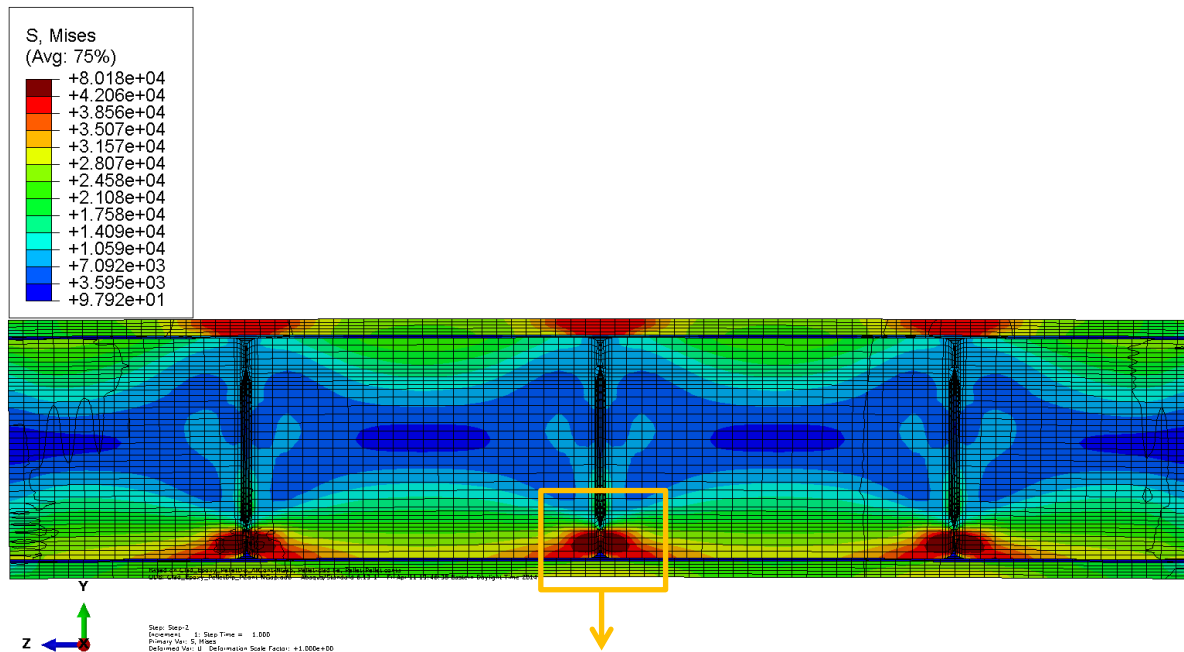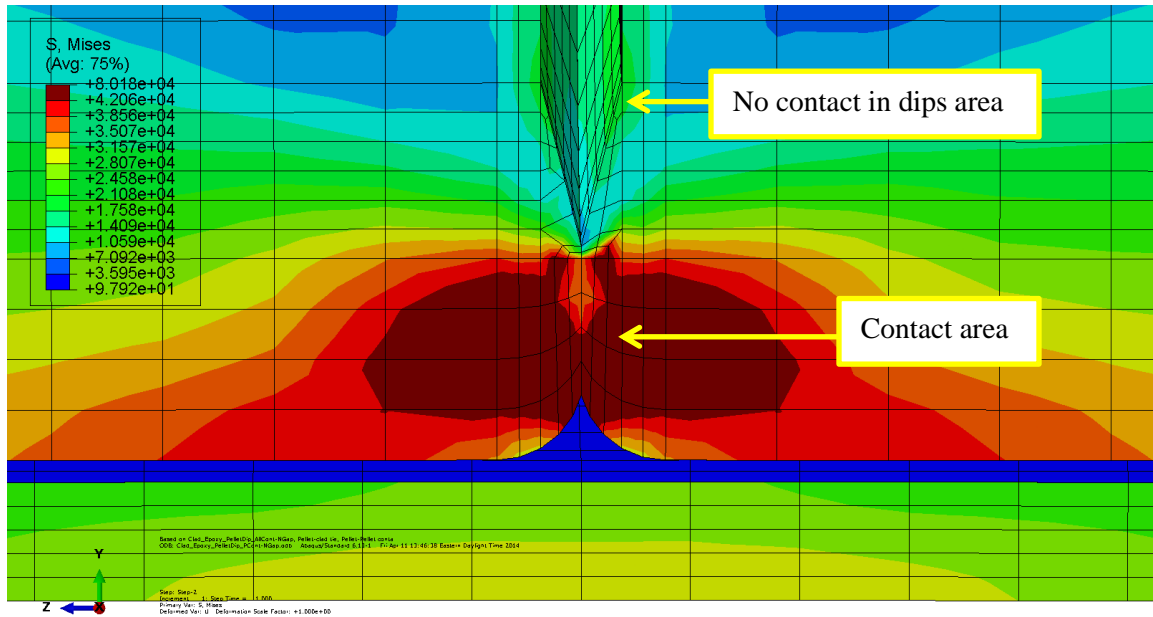Table 3 summarizes the estimated curvature and the flexural rigidity from the four FEA simulation cases discussed in this section. The same bending moment is used in all FEA simulations. The curvature and the flexural rigidity listed in Table 3 indicates that for the perfect interface bonding simulation, the immediate consequence of de-bonding at the pellet-pellet interface is a significant increase in curvature, which results in a significant reduction in the estimated flexural rigidity. This phenomenon is primary due to the load carrying capacity of the system shifting from the pellets to the clad.

Table 3. Curvature and flexural rigidity for bonded pellet-clad interfaces and de-bonded pellet-pellet interfaces

	Curvature κ (1/m)	Bending moment M (N*m)	Flexural rigidity EI (N*m^2)
Clad-Epoxy-Pellet (4)-Pellet-Contact-Gap	0.616	25	40.6
Clad-Epoxy-Pellet (4)-Pellet with dish-Contact-Gap	0.620	25	40.4
Clad-Epoxy-Pellet (4)-Pellet-Contact-no Gap	0.231	25	108.1
Clad-Epoxy-Pellet (4)-Pellet with dish-Contact-no Gap	0.241	25	103.6

The induced curvature of 0.616 m^{-1} for the de-bonded pellet-pellet interfaces with gaps case is 4.6 times the curvature of the perfect bonded with epoxy in the gaps case, which had a curvature of 0.134 m^{-1}. The estimated flexural rigidity of 40.6 N*m^2 for the de-bond pellet-pellet interface simulation is about 78% less than that of 186.4 N*m^2 for the perfect bond interface case.

Table 3 reflects that there is no significant difference between the curvature for pellets with and pellets without dish, especially for the empty gaps between pellet-pellet interfaces case. For the case that pellet surfaces directly contacted each other (no gaps), there is a slight change in curvature because of the contact surface change. This was true in the simulations with and without dish in the end of the pellets. The gaps at pellet-pellet interfaces play a critical role in estimating the flexural rigidity of the surrogate rod. The induced curvature of 0.616 m^{-1} for the de-bonded pellet-pellet interfaces with empty gaps without pellet dish is 2.7 times that of the de-bond pellet-pellet interfaces without gaps, and this results in a 62 % reduction in flexural rigidity from 108.1 N*m^2 of no gaps case to 40.6 N*m^2 of empty gaps case. The scenario of pellet with dish reflects similar impacts when the gaps were eliminated. This indicates that the gap induced large plastic deformations in the SS clad at the pellet-pellet interface region, which can lead to a significant reduction in the bending stiffness, (i.e., the flexural rigidity [EI]) of the surrogate rod system. If there are no gaps at the pellet-pellet interfaces, the pellets can carry a significant portion of the bending moment resistance via direct pellet-pellet contact (interaction) to mitigate the potential yield in the clad.

2.3 De-bonded Pellet-Clad and Pellet-Pellet Interfaces

In addition to the flexural shear stress in the SNF system, under flexural deformation, high shear stress will occur at pellet-clad interfaces as a result of the material mismatch. Thus, under reverse bend loading during normal transportation, both cyclic normal stress and shear stress can degrade the interface bonding at fuel pellet-clad interfaces. In this section, de-bonded pellet-clad interfaces and de-bonded pellet-pellet interface cases are investigated using the Clad-Epoxy-Pellet section model with four pellets. The

surrogate rod consists of SS clad and alumina pellet inserts is used to study the system response to bending moment with de-bonded interfaces. Loading and boundary conditions are the same as that of the previous cases, and bending moment is assigned at 25 N*m.

The first simulation case of interfacial de-bonding for both pellet-clad and pellet-pellet interfaces is illustrated in Fig. 18. There are empty gaps at de-bonded pellet-pellet interfaces and a thin epoxy layer at the de-bonded pellet-clad interfaces. Pellets have flat surfaces with round fillets of 0.002 in.
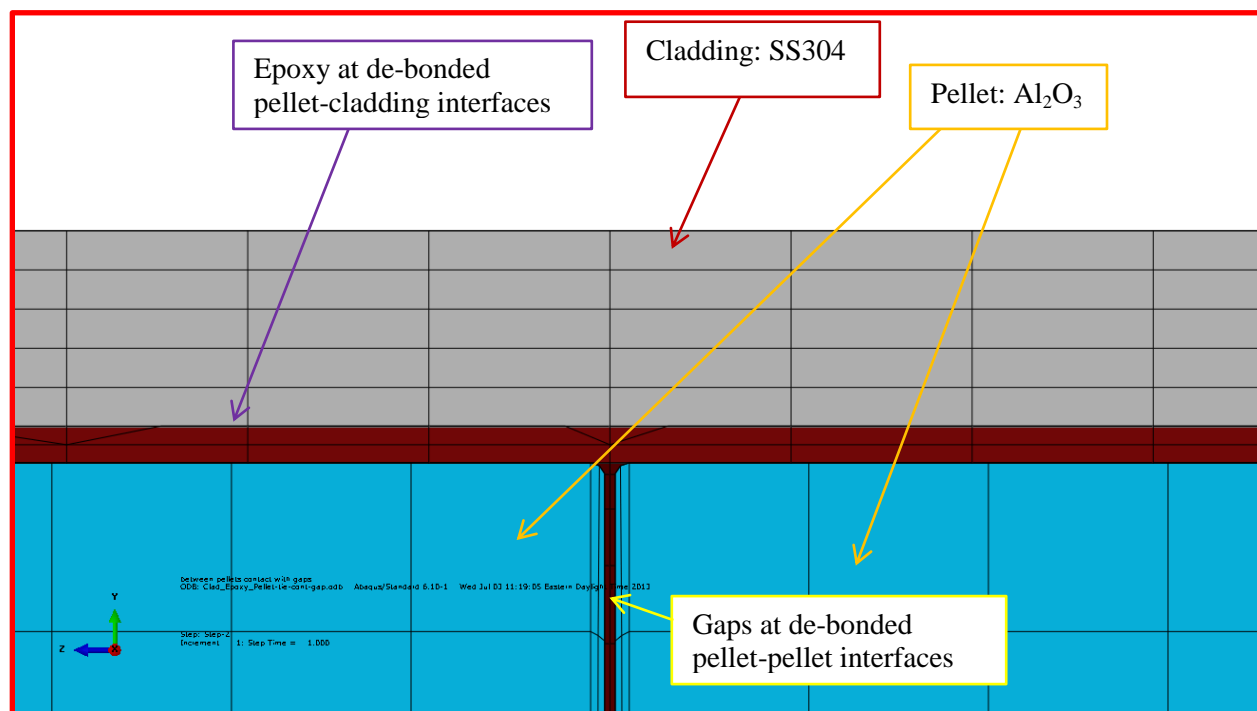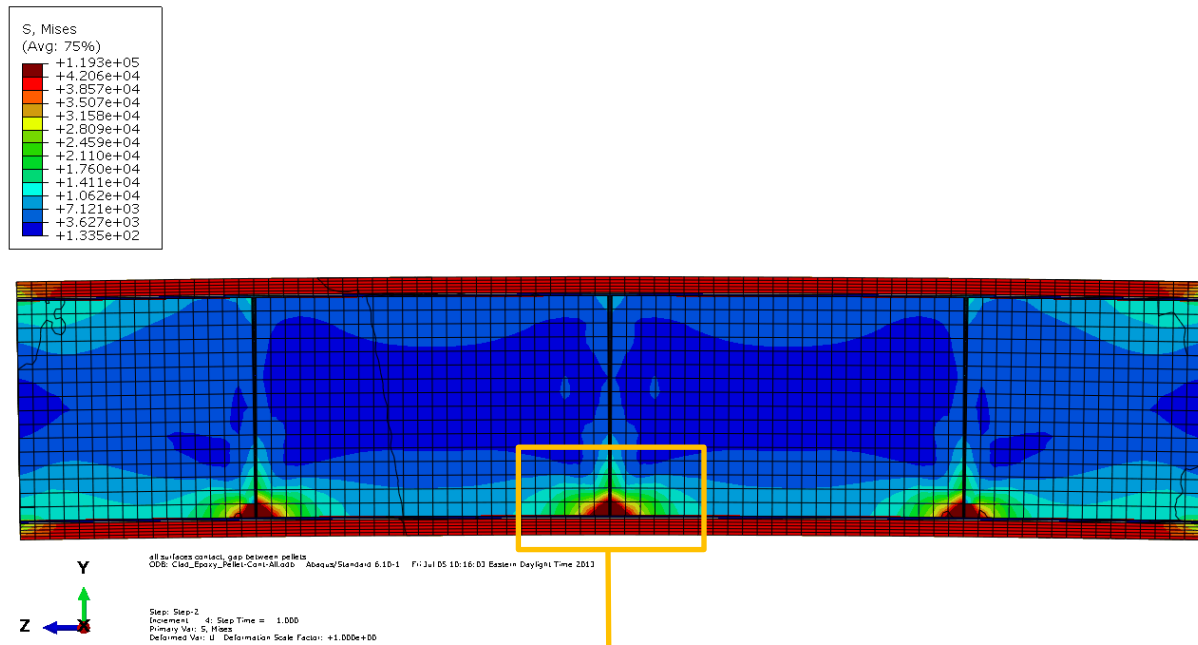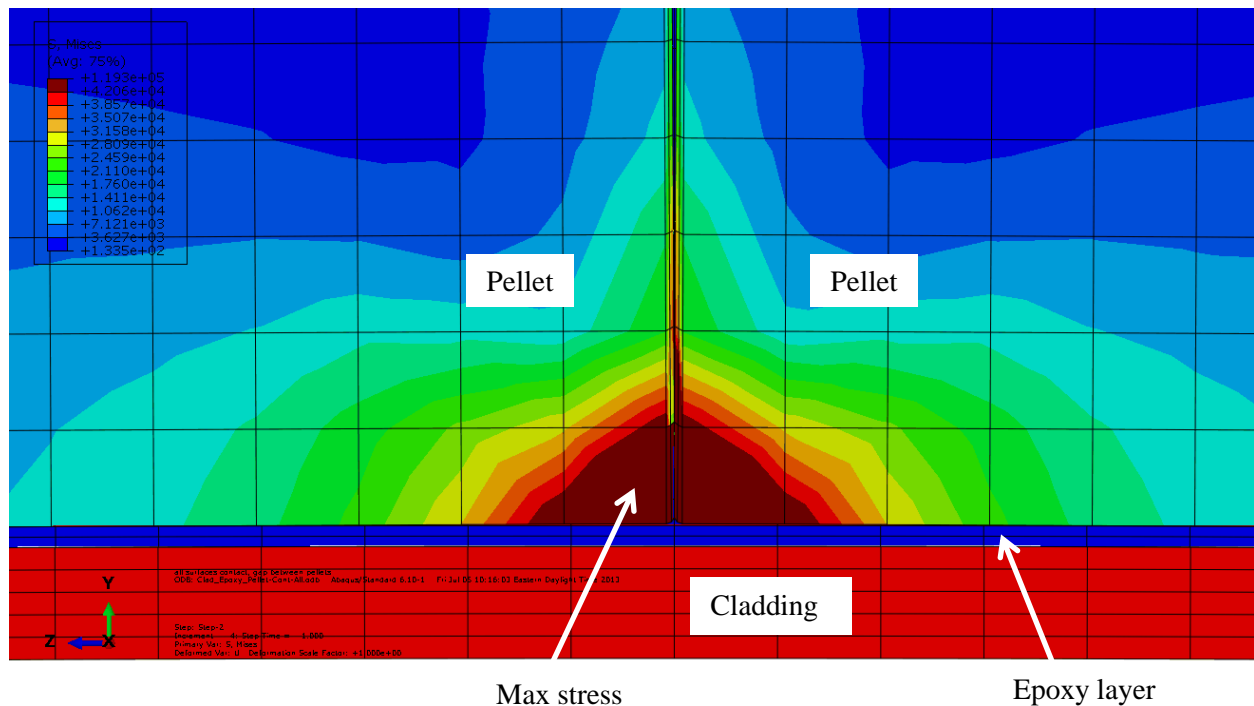

Fig. 20. Enlarged area in Fig. 4 for the case of empty gaps at de-bonded pellet-pellet interfaces and an epoxy filled layer at de-bonded pellet-clad interfaces.

The stress distribution shown in Fig. 21 indicates that when the interfacial de-bonding occurs at both pellet-clad and pellet-pellet interfaces the SS clad yielded throughout the whole gauge section. This is in contrast to results shown in Fig. 15, where the SS clad only yielded locally at the pellet-pellet interface regions, and the maximum stress resides at pellets in the compression side of the pellet-pellet interfaces. The pellets were all below yield at the maximum stress level due to their high yield strength. The pellet stress contours also reflect a dog bone shape due to pellet-pellet contact interaction. The induced curvature of $0.683m^{-1}$ is large enough to be visualized from the longitudinal cut view without increasing the scale. This suggests that due to the interface de-bonding both at pellet-clad and pellet-pellet interfaces, the pellet inserts and the SS clad can only contact (or pin) at the pellet-pellet-clad interface region and pellets cannot provide direct internal support to the clad. Therefore, the load carrying capacity shifts significantly from pellets to the clad in the entire gauge section. The results also indicate that the SS clad carries the majority of the bending moment resistance. The bending deformation in the de-bonded pellet-clad region will likely result in further pining action at pellet-clad interfaces, which may also result in an accelerated aging of the clad tubing.

(a) Longitudinal cut view of resultant curvature and von Mises stress

(b) Enlarged view of stress distribution at pellet-clad pinning region
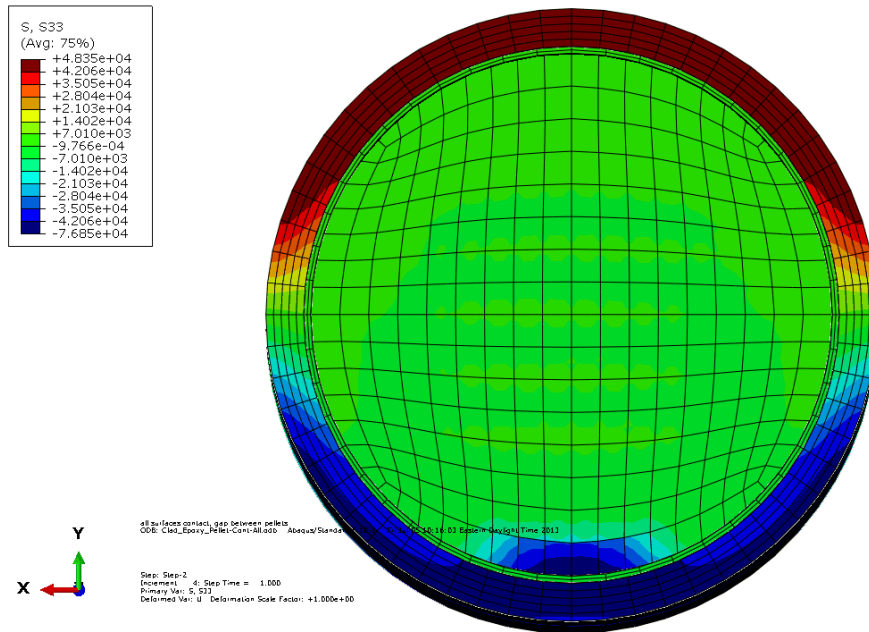
(c) Cross section view of resultant σ_{zz} at a pellet-pellet interface

Fig. 21. The stress distribution and curvature of Clad-Epoxy-Pellet section model of four flat pellets with empty gaps at de-bonded pellet-pellet interfaces and epoxy layer at de-bonded pellet-clad interfaces.

Similar to previous discussions, the second simulation case of interfacial de-bonding for both pellet-clad and pellet-pellet interfaces use the same conditions as described in the first simulation case, except the pellets have dish and round fillets of 0.02 in. at end surfaces.

(a) Longitudinal cut view of resultant curvature and von Mises stress.

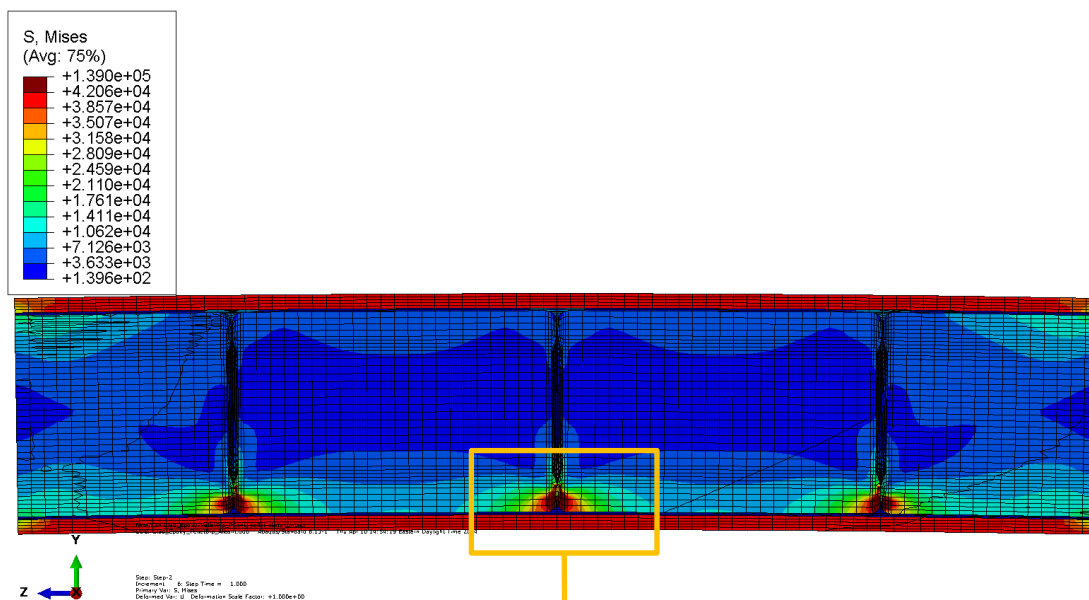*(b) Enlarged view of stress distribution at pellet-clad pinning region*
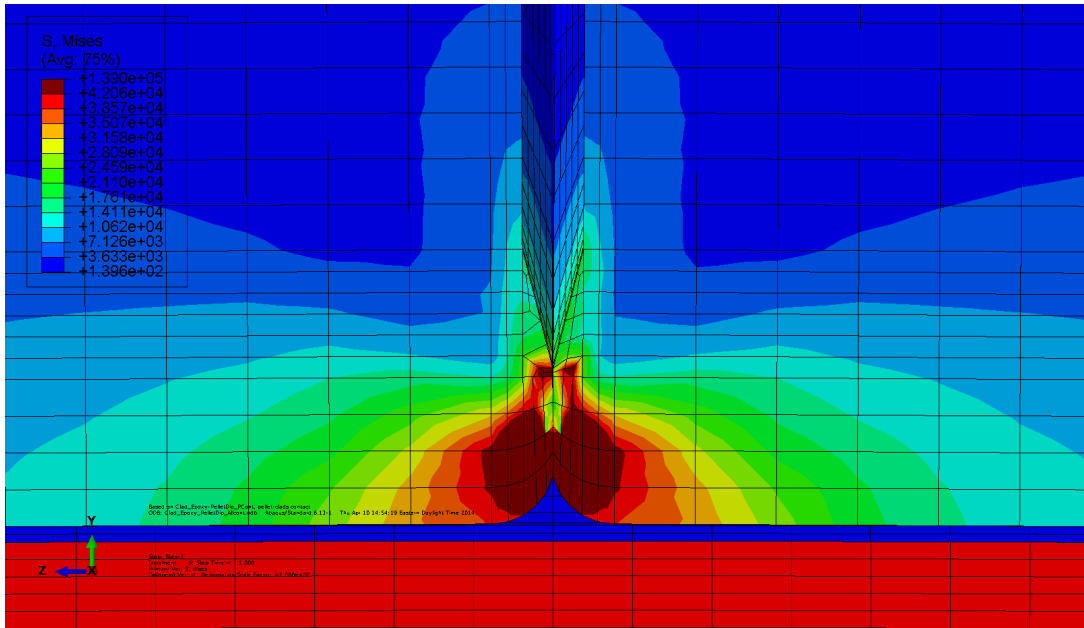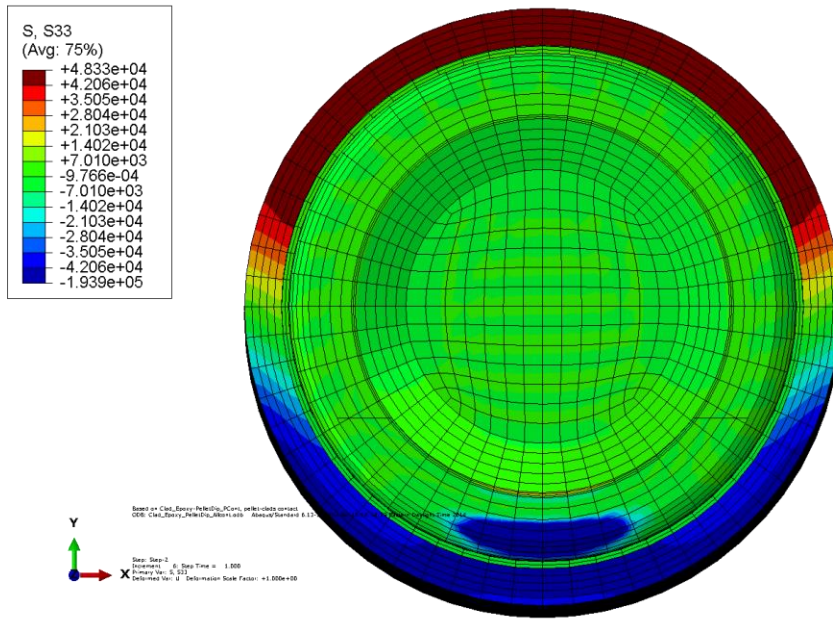

(b) Cross section view of resultant σ$_{zz}$ at a pellet-pellet interface

Fig. 22. The stress distribution and curvature of Clad-Epoxy-Pellet section model of four pellets with dish and with empty gaps at de-bonded pellet-pellet interfaces and epoxy layer at de-bonded pellet-clad interfaces.

The stress distribution in Fig. 22 reflects the similar pattern noted in Fig. 21. All of the cladding has yielded, and maximum stress occurs in the pellet-pellet pinching area. The maximum stress is higher than that seen in the first simulation case due to the reduced contact area due to pellet dish and bigger round at end surfaces. However the maximum stress is still below the pellet material yield strength.

The third case in this section is shown in Fig. 23, where a thin epoxy layer filled the de-bonded pellet-clad interfaces and the pellets are all in direct contact to each other without gaps at pellet-pellet interfaces. The loading and boundary conditions as well as material properties are the same as that of the previous cases. In this case, there are four flat pellets with round 0.002 in.
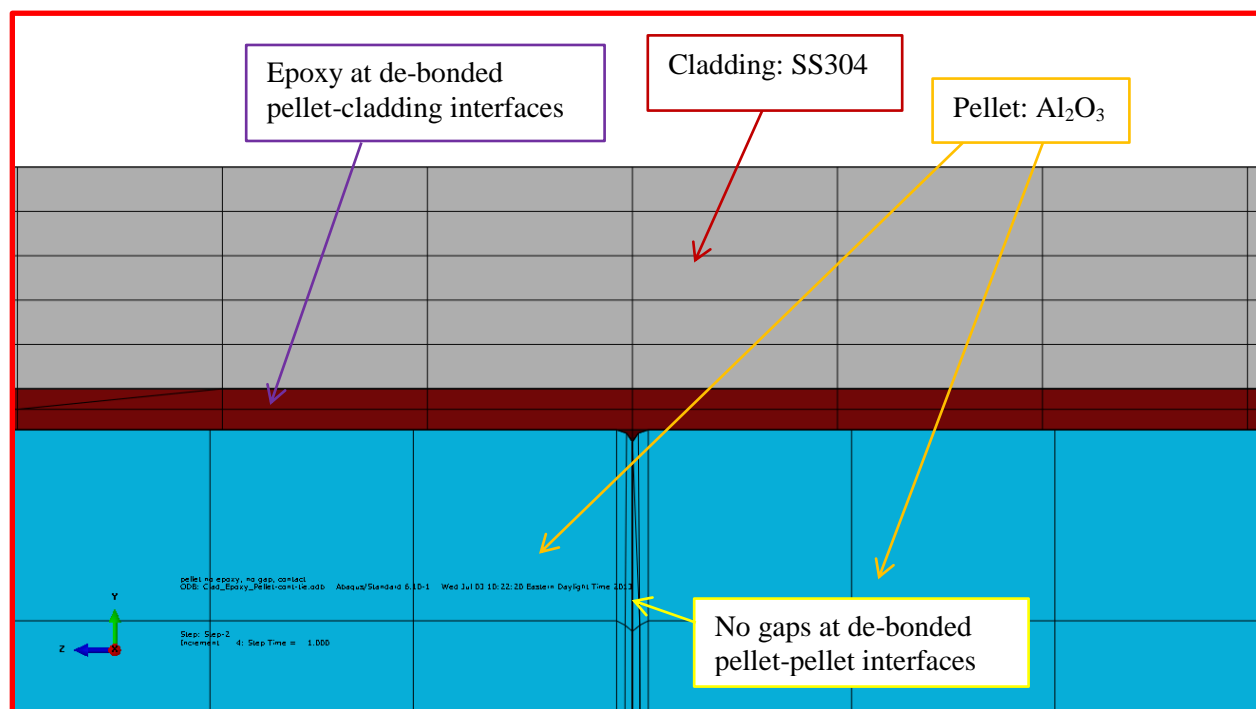
Fig. 23. Enlarged area in Fig. 4 for the case of no gaps at the de-bonded pellet-pellet interfaces and epoxy.

Fig. 24 illustrates the surrogate rod response to the bending moment upon interfacial de-bonding without gaps at pellet-pellet interfaces. The longitudinal cut view shows that the SS clad yields at the top (tension) region throughout the gauge section, but remain elastic at the bottom (compression) region. The maximum stress still occurs at the compression side of pellet region where the pellets are pinning to each other. Fig. 24 shows similar interfacial results observed in Fig. 18 for the bond pellet-clad interfaces and de-bonded pellet-pellet interfaces without gaps. The pellets carry a large portion of the bending moment resistance via the pinching pellet corners and reduce the stress intensity at the bottom (compression) portion of the clad. The major difference compared to the results of Fig. 18 is the extensive plastic deformation observed at the top region of the SS tube throughout the entire gauge section, which differs from the localized yielding observed at the interface region of Fig. 18. The lack of a direct load transferring mechanism from pellet to clad or vice versa due to de-bonding pellet-clad interfaces, means that the clad takes over the majority of the bending moment resistance layer at the de-bonded pellet-clad interfaces.
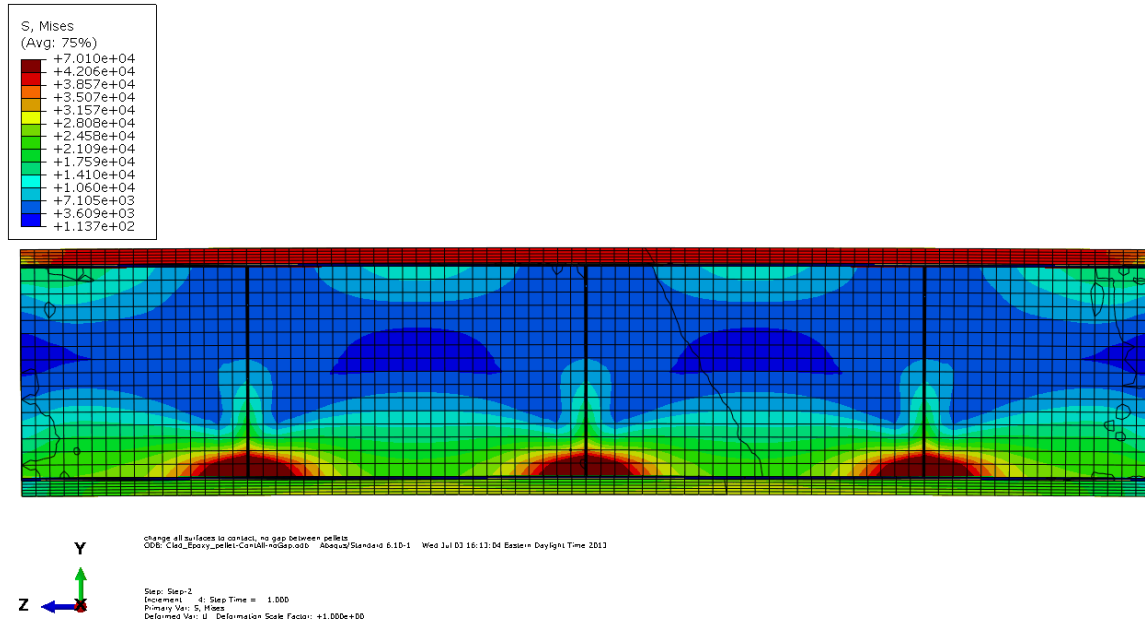
(a) Longitudinal cut view of resultant curvature and von Mises stress
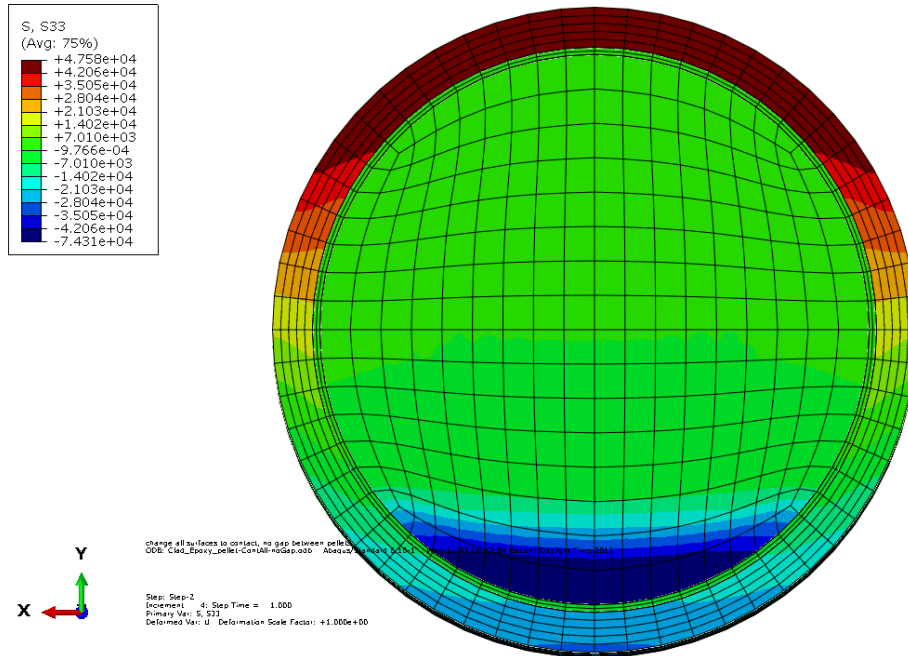
(b) Cross section view of the resultant normal stress, σ_{zz}, at a pellet-pellet interface

Fig. 24. The stress distribution and curvature of Clad-Epoxy-Pellet section model of four flat pellets, with no gaps at de-bonded pellet-pellet interfaces and with epoxy layer at de-bonded pellet-clad interfaces.

The fourth simulation case is similar to the third case as shown in Fig. 23. The pellets have dish in both ends with end surface round fillet of 0.02 in. (same as the second simulation case).

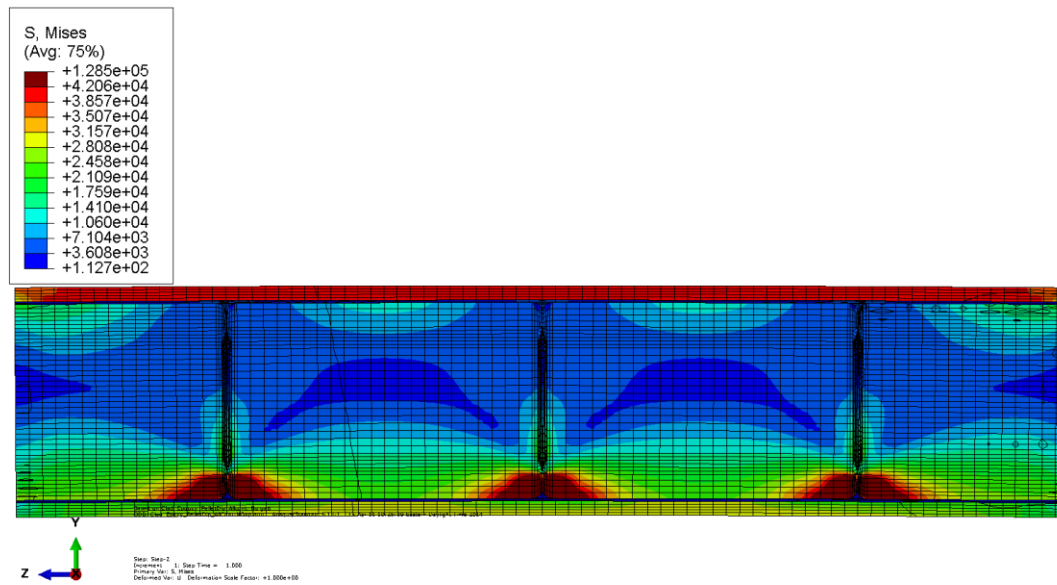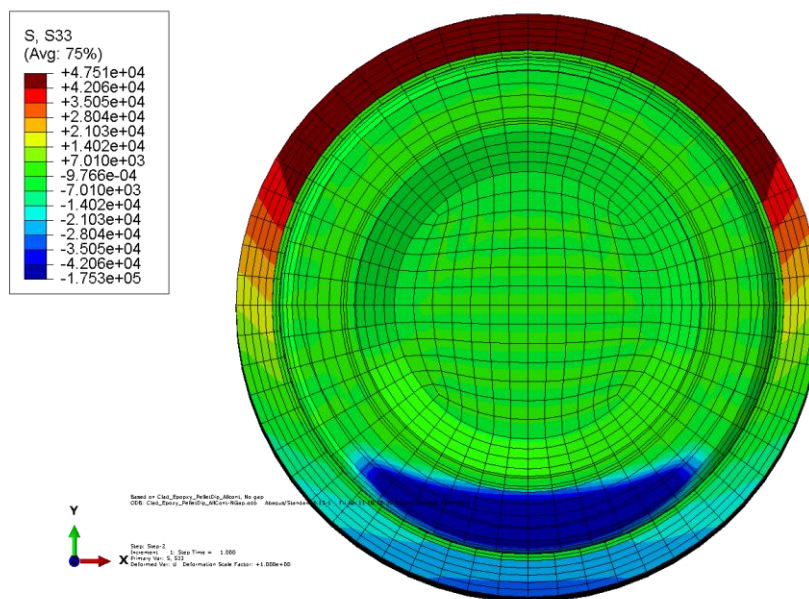*(a) Longitudinal cut view of resultant curvature and von Mises stress*

(b) Cross section view of the resultant normal stress, σ_{zz}, at a pellet-pellet interface

Fig. 25. The stress distribution and curvature of the Clad-Epoxy-Pellet section model of four pellets with dish, without gaps at de-bonded pellet-pellet interfaces and with epoxy layer at de-bonded pellet-clad interfaces

Fig. 25 shows that this simulation had a fairly close stress distribution to the results reflected in Fig. 24. The dish and larger round at the end surfaces of the pellets drive the maximum stress to much higher levels than seen in Fig. 24. The results of the curvature and flexural rigidity evaluated for the cases of de-bonding at pellet-clad and pellet-pellet interfaces are listed in Table 4. Generally, the reduction of contact area with dish and larger round at the end surfaces of the pellets results in the higher curvatures and lower estimated flexural rigidities. The difference is small for the case of with empty gaps between the pellet-pellet interfaces; while the difference is 6% for the case of with no gaps. The gap still plays an important role in the reduction of flexural rigidity. Compared to the results of the de-bonded pellet-pellet interface case listed in Table 3, the flexural rigidities are decreased by 10% in the pellet with gap cases and 19% in the pellet without gap cases. This result further validates the earlier hypothesis that the interface bonding efficiency can significantly affect the flexural rigidity of the surrogate composite rod.

In Table 4, the flexural rigidity of the case with no gaps at the pellet-pellet interfaces is 2.4 times of that of the case with gaps. In Table 3, the ratio of the flexural rigidity is 2.7 in a similar comparison. The reason for the large increase in the flexural rigidity is the direct pellet contact at the pellet-pellet interfaces on the compression side of the rod. The direct pellet-pellet contact interaction also provides a significant increase in bending moment resistance and results in a much less curvature deformation as shown in Table 4.

Table 4. The curvature and flexural rigidity for de-bond pellet-clad and pellet-pellet interfaces

	Curvature κ (1/m)	Bending moment M (N*m)	Flexural rigidity EI (N*m^2)
Clad-Epoxy-Pellet (4)-Contact-Pellet-Contact-Gap	0.683	25	36.6
Clad-Epoxy-Pellet (4)-Contact-Pellet W/dip-Contact-Gap	0.697	25	36.0
Clad-Epoxy-Pellet (4)-Contact-Pellet-Contact-no Gap	0.287	25	87.2
Clad-Epoxy-Pellet (4)-Contact-Pellet W/Dip-Contact-no Gap	0.306	25	81.6

3. CONCLUSION

Based on the FEA simulation results and on verification from ORNL surrogate rod bending test results, the impacts of interfacial bonding efficiency at pellet-pellet and pellet-clad interfaces for surrogate rod system performance can be summarized as follows.

First, with good interface bonding and without fuel pellet and clad fracture, the pellets in the surrogate rod will carry more bending moment resistance than the clad under normal transportation vibration. The maximum stress resides with the pellets and the stresses at the clad and pellet are both below the yield condition; therefore, the system is in a linear elastic state under the target bending loads. Due to the dish in the end of the pellets and bigger round fillets at the end surfaces, contact surface is minimized to a limited area and the maximum stress is higher than that of pellets with flat surfaces. However, the flexural rigidity of pellets with dish is much smaller than that of pellets with flat surfaces.

With fuel pellet failure, including de-bonding at the pellet-pellet interfaces, the load carrying capacity shifts from fuel pellets to the clad, and the clad starts to carry the majority of the bending moment at the

pellet-pellet interface region, which results in localized plastic deformation of the clad. With good cohesive bonding at the pellet-clad interfaces, the pellets can still provide support to the clad and carry a sufficient portion of the bending moment resistance, so the major portion of the clad at the gauge section remains in the linear elastic range. The dish of pellets has very limited impact on the estimated flexural rigidity, especially with the gaps between the pellet-pellet interfaces. The reduction of contact surfaces drives the maximum stress higher.

With increased de-bonding at the pellet-clad interfaces, the pellets can no longer provide effective structural support to the clad nor assist the load transfer within the surrogate rod system. Thus, the majority of the load carrying capacity shifts to the clad throughout the entire gauge section. That leads to the clad yielding in the entire gauge section instead of at localized pellet-pellet interface regions. When the pellets contact and pinch each other, the pellets seem to take over a significant portion of the bending load resistance, especially in cases where there are no gaps at the pellet-pellet interfaces. This pellet pining action certainly mitigates and prevents the clad yielding and the maximum stress resides in the pellet region and remains below the yield.

The effect of the pellets fabricated with dish was shown in Table 5, where the maximum difference between pellets with flat surfaces and pellets with dish is 15% for the perfect bond condition because of the reduction of contact surface due to the dish area. At de-bonded interfaces with gaps, the impacts of dish are small enough to be neglected. At de-bonded interfaces without gaps, the difference is around 4-6%.

The immediate consequence of interface de-bonding is the load carrying capacity shift from fuel to clad, as well as the reduction of system flexural rigidity. Compared to the flexural rigidity of 158 N*m^2 for a perfect bond of pellet with dish, de-bonding at the pellet-pellet interfaces reduces flexural rigidity by 74% to 40.4 N*m^2 in the case with gaps at the pellet-pellet interfaces and by 34% to 103.4 N*m^2 for the case with no gaps. Upon further de-bonding at the pellet-clad interfaces, the flexural rigidity reduces by 11% and 21% for the case with gaps and without gaps, respectively. The overall reductions from the perfect bond case to the de-bonded case at all interfaces are about 77% and 48%, respectively, for the cases with gaps and without gaps.

There are more reductions in the flexural rigidities due to de-bonding at pellet-pellet interfaces than due to de-bonding at pellet-clad interfaces. Table 5 shows about 60% increase in the flexural rigidity from the case with gaps to the case without gaps, which indicates a significant increase in system stiffness for the surrogate rod without gaps. Therefore, the gaps at the interfaces of the surrogate rod system can have a significant impact to the system reliability, especially at pellet-pellet interfaces.

The flexural rigidity and bending moment resistance capacity of the surrogate rod system (which is designed to resemble the SNF system) are strongly dependent on interface bonding efficiency at pellet-clad and pellet-pellet interfaces. This discovery was also validated from ORNL CIRFT test results performed on the surrogate SS rod with alumina pellets inserts.

The FEA results of the surrogate rod system with gaps at interfaces reveal very similar results for the case of full system de-bonding and for the case of de-bonded pellet-pellet interfaces only. The variation of pellet position at the gauge section has little impact to the surrogate rod system response under bending loads. The FEA results using displacement-control procedure is consistent to that of using load control approach.

Table 5. The flexural rigidity comparison between the different bonding and de-bonding cases

	Flexural rigidity EI (N*m²)	Reduction from flat surface to dips (%)	Reduction from perfect bond (%)	Reduction from only pellet-pellet de-bond to further pellet-clad de-bond (%)	Increase from with gaps to without gaps (%)
Perfect bond of pellet with flat surfaces	186				
Perfect bond of pellet with dips	158	15			
De-bonded Pellet-Pellet Interfaces with Gaps, pellet with flat surfaces	40.6		78		
De-bonded Pellet-Pellet Interfaces with Gaps, pellet with dips	40.4	0.5	74		
De-bonded Pellet-Pellet and Pellet-Clad Interfaces with Gaps, pellet with flat surfaces	36.6		80	7	
De-bonded Pellet-Pellet and Pellet-Clad Interfaces with Gaps, pellet with dips	36.0	1.6	77	11	
De-bonded Pellet-Pellet interfaces without Gaps, pellet with flat surfaces	108.1		42		62
De-bonded Pellet-Pellet interfaces without Gaps, pellet with dish	103.6	4	34		61
De-bonded Pellet-Pellet and Pellet-Clad Interfaces without Gaps, pellet with flat surfaces	87.2		53	19	58
De-bonded Pellet-Pellet and Pellet-Clad Interfaces without Gaps, pellet with dish	81.6	6	48	21	56

4. REFERENCES

1. U.S. Department of Energy Used Fuel Disposition Campaign, *Used Nuclear Fuel Loading and Structural Performance Under Normal Conditions of Transport - Modeling, Simulation and Experimental Integration RD&D Plan*, FCRD-UFD-2013-000135, April 1, 2013.

2.   J.-A. J. Wang, H. Wang, Y. Yan, R. Howard, and B. Bevard, *High Burn-up Spent Fuel Vibration Integrity Study Progress Letter Report* (Out-of-Cell Fatigue Testing Development – Task 2.1), ORNL/TM-2010/288, Oak Ridge National Laboratory, Oak Ridge, TN, 2011.

3. J.-A. J. Wang, H. Wang, T. Tan, H. Jiang, T. Cox, and Y. Yan, *Progress Letter Report on U-frame Test Setup and Bending Fatigue Test for Vibration Integrity Study* (Out-of-Cell Fatigue Testing Development – Task 2.2), ORNL/TM-2011/531, Oak Ridge National Laboratory, Oak Ridge, TN, 2012.

4. H. Wang, J.-A. J. Wang, T. Tan, H. Jiang, T. Cox, R. Howard, B. Bevard, and M. Flanagan, "Development of U-Frame Bending System for Studying the Vibration Integrity of Spent Nuclear Fuel," *Journal of Nuclear Material*, **440**, 201-213, 2013.

5. Product Data Bulletin, 304/304L stainless steel, AK Steel Corporation, http://www.aksteel.com.

6. Ceramic Properties Standard, CoorsTek, Inc., http://www.coorstek.com.

7. More About Glass, Ceramics, Carbon, More About Stainless Steel Alloys, Mechanical and Physical Properties, http://www.mcmaster.com.

8. http://www.engineeringtoolbox.com/engineering-materials-propertiesd_1225.html.